Inverse Compton emission revealed by multi-wavelength observations of a gamma-ray burst

The MAGIC Collaboration: V. A. Acciari[1], S. Ansoldi[2,21], L. A. Antonelli[3], A. Arbet Engels[4], D. Baack[5], A. Babić[6], B. Banerjee[7], U. Barres de Almeida[8], J. A. Barrio[9], J. Becerra González[1], W. Bednarek[10], L. Bellizzi[11], E. Bernardini[12,16], A. Berti[13], J. Besenrieder[14], W. Bhattacharyya[12], C. Bigongiari[3], A. Biland[4], O. Blanch[15], G. Bonnoli[11], Ž. Bošnjak[6], G. Busetto[16], R. Carosi[17], G. Ceribella[14], Y. Chai[14], A. Chilingaryan[22], S. Cikota[6], S. M. Colak[15], U. Colin[14], E. Colombo[1], J. L. Contreras[9], J. Cortina[25], S. Covino[3], V. D'Elia[3], P. Da Vela[17], F. Dazzi[3], A. De Angelis[16], B. De Lotto[2], M. Delfino[15,27], J. Delgado[15,27], D. Depaoli[13], F. Di Pierro[13], L. Di Venere[13], E. Do Souto Espiñeira[15], D. Dominis Prester[6], A. Donini[2], D. Dorner[18], M. Doro[16], D. Elsaesser[5], V. Fallah Ramazani[19], A. Fattorini[5], G. Ferrara[3], D. Fidalgo[9], L. Foffano[16], M. V. Fonseca[9], L. Font[20], C. Fruck[14], S. Fukami[21], R. J. García López[1], M. Garczarczyk[12], S. Gasparyan[22], M. Gaug[20], N. Giglietto[13], F. Giordano[13], N. Godinović[6], D. Green[14], D. Guberman[15], D. Hadasch[21], A. Hahn[14], J. Herrera[1], J. Hoang[9], D. Hrupec[6], M. Hütten[14], T. Inada[21], S. Inoue[21], K. Ishio[14], Y. Iwamura[21], L. Jouvin[15], D. Kerszberg[15], H. Kubo[21], J. Kushida[21], A. Lamastra[3], D. Lelas[6], F. Leone[3], E. Lindfors[19], S. Lombardi[3], F. Longo[2,26,30], M. López[9], R. López-Coto[16], A. López-Oramas[1], S. Loporchio[13], B. Machado de Oliveira Fraga[8], C. Maggio[20], P. Majumdar[7], M. Makariev[23], M. Mallamaci[16], G. Maneva[23], M. Manganaro[6], K. Mannheim[18], L. Maraschi[3], M. Mariotti[16], M. Martínez[15], D. Mazin[14,21], S. Mićanović[6], D. Miceli[2], M. Minev[23], J. M. Miranda[11], R. Mirzoyan[14], E. Molina[24], A. Moralejo[15], D. Morcuende[9], V. Moreno[20], E. Moretti[15], P. Munar-Adrover[20], V. Neustroev[19], C. Nigro[12], K. Nilsson[19], D. Ninci[15],

K. Nishijima[21], K. Noda[21], L. Nogués[15], S. Nozaki[21], S. Paiano[16], M. Palatiello[2], D. Paneque[14], R. Paoletti[11], J. M. Paredes[24], P. Peñil[9], M. Peresano[2], M. Persic[2], P. G. Prada Moroni[17], E. Prandini[16], I. Puljak[6], W. Rhode[5], M. Ribó[24], J. Rico[15], C. Righi[3], A. Rugliancich[17], L. Saha[9], N. Sahakyan[22], T. Saito[21], S. Sakurai[21], K. Satalecka[12], K. Schmidt[5], T. Schweizer[14], J. Sitarek[10], I. Šnidarić[6], D. Sobczynska[10], A. Somero[1], A. Stamerra[3], D. Strom[14], M. Strzys[14], Y. Suda[14], T. Surić[6], M. Takahashi[21], F. Tavecchio[3], P. Temnikov[23], T. Terzić[6], M. Teshima[14,21], N. Torres-Albà[24], L. Tosti[magic:13], V.Vagelli[magic:13], J. van Scherpenberg[14], G. Vanzo[1], M. Vazquez Acosta[1], C. F. Vigorito[13], V. Vitale[13], I. Vovk[14], M. Will[14], D. Zarić[6]& L. Nava[3,29,30],

For the Fermi Gamma-ray Burst (GBM) team:

P. Veres[43], P. N. Bhat[43], M. S. Briggs[43,44], W. H. Cleveland[42], R. Hamburg[43,44], C. M. Hui[38], B. Mailyan[43], R. D. Preece[43,44], O. Roberts[42], A. von Kienlin[45], C. A. Wilson-Hodge[38],

For the Fermi Large Area Telescope (LAT) collaboration:

D. Kocevski[38], M. Arimoto[31], D. Tak[79,106], K. Asano[32], M. Axelsson[33,34], G. Barbiellini[29], E. Bissaldi[35,36], R. Gill[37], J. Granot[37], J. McEnery[79,106], N. Omodei[39], F. Piron[40], J. L. Racusin[106], S. Razzaque[41], D. J. Thompson[106],

For the Swift collaboration:

S. Campana[46], M. G. Bernardini[46], N. P. M. Kuin[47], M. H. Siegel[48], S. Bradley Cenko[106,49], P. OBrien[65], A. DAì[50], M. De Pasquale[51], J. Gropp[48], N. Klingler[48], J. P. Osborne[65], M. Perri[56,55],

R. Starling[65], G. Tagliaferri[46,50], A. Tohuvavohu[48],

For the AGILE collaboration:

A. Ursi[52], M. Tavani[52,53,54], M. Cardillo [52], C. Casentini [52], G. Piano[52], Y. Evangelista[52],

F. Verrecchia[55,56], C. Pittori [55,56], F. Lucarelli [55,56], A. Bulgarelli [57], N. Parmiggiani [57],

and

G. E. Anderson[67], J. P. Anderson[60], G. Bernardi[76,77,78], J. Bolmer[45], M. D. Caballero-García[84],

I. M. Carrasco[85], A. Castellón[86], N. Castro Segura[116], A. J. Castro-Tirado[58,81], S. V. Cherukuri[72],

A. M. Cockeram[64], P. D'Avanzo[46], A. Di Dato[98,99], R. Diretse[93], R.P. Fender[90],

E. Fernández-García[58], J. P. U. Fynbo[112,113], A.S. Fruchter[111] J. Greiner[45], M. Gromadzki[117], K.E.

Heintz[114] I. Heywood[90,77], A.J. van der Horst[91,92], Y.-D. Hu[58,83], C. Inserra[103], L. Izzo[58,59],

V. Jaiswal[72], P. Jakobsson[114], J. Japelj[124], E. Kankare[102], D. A. Kann[58], C. Kouveliotou[91,92],

S. Klose[71], A. J. Levan[110], X. Y. Li[87,88], S. Lotti[52], K. Maguire[104], D. B. Malesani[122,112,113,59],

I. Manulis[101], M. Marongiu[75,125], S. Martin[60,61], A. Melandri[46], M. Michałowski[62],

J.C.A. Miller-Jones[67], K. Misra[73,74], A. Moin[68], K.P. Mooley[96,97], S. Nasri[68], M. Nicholl[118,119],

A. Noschese[98], G. Novara[107,108], S. B. Pandey[73], C. J. Pérez del Pulgar[81], M.A. Pérez-Torres[58,95],

D. A. Perley[64], L. Piro[52], F. Ragosta[120,121,99], L. Resmi[72], R. Ricci[76] A. Rossi[105],

R. Sánchez-Ramírez[52], J. Selsing[113] S. Schulze[66], S. J. Smartt[100], I. A. Smith[63], V. V. Sokolov[82],

J. Stevens[70], N. R. Tanvir[65], C. C. Thoene[58], A. Tiengo[107,108,109], E. Tremou[89], E. Troja[106,80],

A. de Ugarte Postigo[58,59], A. F. Valeev[82], S. D. Vergani[94], M. Wieringa[69], P.A. Woudt[93], D. Xu[123],

O. Yaron[101], D. R. Young[100],

[1]*Inst. de Astrofísica de Canarias, E-38200 La Laguna, and Universidad de La Laguna, Dpto. Astrofísica, E-38206 La Laguna, Tenerife, Spain*

[2]*Università di Udine, and INFN Trieste, I-33100 Udine, Italy*

[3]*National Institute for Astrophysics (INAF), I-00136 Rome, Italy*

[4]*ETH Zurich, CH-8093 Zurich, Switzerland*

[5]*Technische Universität Dortmund, D-44221 Dortmund, Germany*

[6]*Croatian Consortium: University of Rijeka, Department of Physics, 51000 Rijeka; University of Split - FESB, 21000 Split; University of Zagreb - FER, 10000 Zagreb; University of Osijek, 31000 Osijek; Rudjer Boskovic Institute, 10000 Zagreb, Croatia*

[7]*Saha Institute of Nuclear Physics, HBNI, 1/AF Bidhannagar, Salt Lake, Sector-1, Kolkata 700064, India*

[8]*Centro Brasileiro de Pesquisas Físicas (CBPF), 22290-180 URCA, Rio de Janeiro (RJ), Brasil*

[9]*Unidad de Partículas y Cosmología (UPARCOS), Universidad Complutense, E-28040 Madrid, Spain*

[10]*University of Łódź, Department of Astrophysics, PL-90236 Łódź, Poland*

[11]*Università di Siena and INFN Pisa, I-53100 Siena, Italy*

[12]*Deutsches Elektronen-Synchrotron (DESY), D-15738 Zeuthen, Germany*

[13]*Istituto Nazionale Fisica Nucleare (INFN), 00044 Frascati (Roma) Italy*

[14]*Max-Planck-Institut für Physik, D-80805 München, Germany*

[15]*Institut de Física d'Altes Energies (IFAE), The Barcelona Institute of Science and Technology (BIST), E-08193 Bellaterra (Barcelona), Spain*

[16] *Università di Padova and INFN, I-35131 Padova, Italy*

[17] *Università di Pisa, and INFN Pisa, I-56126 Pisa, Italy*

[18] *Universität Würzburg, D-97074 Würzburg, Germany*

[19] *Finnish MAGIC Consortium: Finnish Centre of Astronomy with ESO (FINCA), University of Turku, FI-20014 Turku, Finland; Astronomy Research Unit, University of Oulu, FI-90014 Oulu, Finland*

[20] *Departament de Física, and CERES-IEEC, Universitat Autònoma de Barcelona, E-08193 Bellaterra, Spain*

[21] *Japanese MAGIC Consortium: ICRR, The University of Tokyo, 277-8582 Chiba, Japan; Department of Physics, Kyoto University, 606-8502 Kyoto, Japan; Tokai University, 259-1292 Kanagawa, Japan; RIKEN, 351-0198 Saitama, Japan*

[22] *The Armenian Consortium: ICRANet-Armenia at NAS RA, A. Alikhanyan National Laboratory*

[23] *Inst. for Nucl. Research and Nucl. Energy, Bulgarian Academy of Sciences, BG-1784 Sofia, Bulgaria*

[24] *Universitat de Barcelona, ICCUB, IEEC-UB, E-08028 Barcelona, Spain*

[25] *Centro de Investigaciones Energticas, Medioambientales y Tecnolgicas, E-28040 Madrid, Spain*

[26] *also at Dipartimento di Fisica, Università di Trieste, I-34127 Trieste, Italy*

[27] *also at Port d'Informació Científica (PIC) E-08193 Bellaterra (Barcelona) Spain*

[28] *Centro de Investigaciones Energéticas, Medioambientales y Tecnológicas, E-28040 Madrid, Spain*

[29] *Istituto Nazionale di Fisica Nucleare, Sezione di Trieste, I-34149 Trieste, Italy*

[30] *Institute for Fundamental Physics of the Universe (IFPU), I-34151 Trieste, Italy*

[31] *Faculty of Mathematics and Physics, Institute of Science and Engineering, Kanazawa University, Kakuma, Kanazawa, Ishikawa 920-1192*

[32] *Institute for Cosmic-Ray Research, University of Tokyo, 5-1-5 Kashiwanoha, Kashiwa, Chiba, 277-8582, Japan*

[33] *Department of Physics, Stockholm University, AlbaNova, SE-106 91 Stockholm, Sweden*

[34] *Department of Physics, KTH Royal Institute of Technology, AlbaNova, SE-106 91 Stockholm, Sweden*

[35] *Dipartimento di Fisica "M. Merlin" dell'Università e del Politecnico di Bari, I-70126 Bari, Italy*

[36] *Istituto Nazionale di Fisica Nucleare, Sezione di Bari, I-70126 Bari, Italy*

[37] *Department of Natural Sciences, Open University of Israel, 1 University Road, POB 808, Ra'anana 43537, Israel*

[38] *Astrophysics Office, ST12, NASA/Marshall Space Flight Center, Huntsville, AL 35812, USA*

[39] *W. W. Hansen Experimental Physics Laboratory, Kavli Institute for Particle Astrophysics and Cosmology, Department of Physics and SLAC National Accelerator Laboratory, Stanford University, Stanford, CA 94305, USA*

[40] *Laboratoire Univers et Particules de Montpellier, Université Montpellier, CNRS/IN2P3, F-34095 Montpellier, France*

[41] *Department of Physics, University of Johannesburg, PO Box 524, Auckland Park 2006, South Africa*

[42]*Science and Technology Institute, Universities Space Research Association, Huntsville, AL 35805, USA*

[43]*Center for Space Plasma and Aeronomic Research, University of Alabama in Huntsville, 320 Sparkman Drive, Huntsville, AL 35899, USA*

[44]*Space Science Department, University of Alabama in Huntsville, 320 Sparkman Drive, Huntsville, AL 35899, USA*

[45]*Max-Planck Institut für extraterrestrische Physik, Giessenbachstraße 1, 85748 Garching, Germany*

[46]*INAF - Astronomical Observatory of Brera, I-23807 Merate (LC), Italy*

[47]*Mullard Space Science Laboratory, University College London, Holmbury St. Mary, Dorking, RH5 6NT, United Kingdom*

[48]*Department of Astronomy and Astrophysics, Pennsylvania State University. 525 Davey Laboratory, University Park, PA 16802, USA*

[49]*Joint Space-Science Institute, University of Maryland, College Park, Maryland 20742, USA*

[50]*INAF Istituto di Astrofisica Spaziale e Fisica Cosmica di Palermo, via Ugo La Malfa 153, I-90146 Palermo, Italia*

[51]*Department of Astronomy and Space Sciences, Istanbul University, Fatih, 34119, Istanbul, Turkey*

[52]*INAF-IAPS, via del Fosso del Cavaliere 100, I-00133 Roma, Italy*

[53]*Univ. "Tor Vergata", Via della Ricerca Scientifica 1, I-00133 Roma, Italy*

[54]*Gran Sasso Science Institute, viale Francesco Crispi 7, I-67100 L'Aquila, Italy*

[55]*INAF-Osservatorio Astronomico di Roma, Via Frascati 33, I-00078 Monteporzio Catone, Italy*

[56]*Space Science Data Center (SSDC), Agenzia Spaziale Italiana (ASI), via del Politecnico s.n.c., I-00133, Roma, Italy*

[57]*INAF-OAS, Bologna, Italy*

[58]*Instituto de Astrofísica de Andalucía (IAA-CSIC), Glorieta de la Astronomía, s/n, E-18008, Granada, Spain*

[59]*DARK, Niels Bohr Institute, University of Copenhagen, Lyngbyvej 2, DK-2100 Copenhagen Ø, Denmark*

[60]*European Southern Observatory, Alonso de Còrdova, 3107, Vitacura, Santiago 763-0355, Chile*

[61]*Joint ALMA Observatory, Alonso de Còrdova, 3107, Vitacura, Santiago 763-0355, Chile*

[62]*Astronomical Observatory Institute, Faculty of Physics, Adam Mickiewicz University, ul. Słoneczna 36, 60-286 Poznań, Poland*

[63]*Department of Physics and Astronomy, Rice University, 6100 South Main, MS-108, Houston, TX 77251-1892, USA*

[64]*Astrophysics Research Institute, Liverpool John Moores University, 146 Brownlow Hill, Liverpool L3 5RF, UK*

[65]*Department of Physics and Astronomy, University of Leicester, University Road, Leicester LE1 7RH, UK*

[66]*Department of Particle Physics and Astrophysics, Weizmann Institute of Science, Rehovot 76100, Israel*

[67]*International Centre for Radio Astronomy Research, Curtin University, GPO Box U1987, Perth,*

WA 6845, Australia

[68]*Physics Department, United Arab Emirates University, P.O. Box 15551, Al-Ain, United Arab Emirates*

[69]*Australia Telescope National Facility, CSIRO Astronomy and Space Science, PO Box 76, Epping, NSW 1710, Australia*

[70]*CSIRO Australia Telescope National Facility, Paul Wild Observatory, Narrabri NSW 2390, Australia*

[71]*Thüringer Landessternwarte Tautenburg, Sternwarte 5, 07778 Tautenburg, Germany*

[72]*Indian Institute of Space Science & Technology, Trivandrum 695547, India*

[73]*Aryabhatta Research Institute of Observational Sciences, Manora Peak, Nainital 263 001, India*

[74]*Department of Physics, University of California, 1 Shields Ave, Davis, CA 95616-5270, USA*

[75]*Department of Physics and Earth Science, University of Ferrara, via Saragat 1, I-44122, Ferrara, Italy*

[76]*INAF-Istituto di Radioastronomia, via Gobetti 101, I-40129, Bologna, Italy*

[77]*Department of Physics and Electronics, Rhodes University, PO Box 94, Grahamstown, 6140, South Africa*

[78]*South African Radio Astronomy Observatory, Black River Park, 2 Fir Street, Observatory, Cape Town, 7925, South Africa*

[79]*Department of Physics, University of Maryland, College Park, MD 20742-4111, USA*

[80]*Department of Astronomy, University of Maryland, College Park, MD 20742-4111, USA*

[81]*Unidad Asociada Departamento de Ingeniería de Sistemas y Automática, E.T.S. de Ingenieros*

Industriales, Universidad de Málaga, Arquitecto Francisco Peñalosa 6, E-29071 Málaga, Spain

[82]*Special Astrophysical Observatory, Nizhniy Arkhyz, Zelenchukskiy region, Karachai-Cherkessian Republic, 369167, Russia*

[83]*Universidad de Granada, Facultad de Ciencias Campus Fuentenueva S/N CP 18071 Granada, Spain*

[84]*Astronomical Institute of the Academy of Sciences, Boční II 1401, CZ-14100 Praha 4, Czech Republic*

[85]*Departamento de Física Aplicada, Facultad de Ciencias, Universidad de Málaga, Bulevar Louis Pasteur 31, E-29071 Málaga, Spain*

[86]*Departamento de Álgebra, Geometría y Topología, Facultad de Ciencias, Bulevar Louis Pasteur 31, Universidad de Málaga, E-29071 Málaga, Spain*

[87]*Instituto de Hortofruticultura Subtropical y Mediterránea La Mayora (IHSM/UMA-CSIC), Algarrobo Costa s/n, E-29750 Málaga, Spain*

[88]*Nanjing Institute for Astronomical Optics and Technology, National Observatories, Chinese Academy of Sciences, 188 Bancang St, Xuanwu Qu, Nanjing Shi, Jiangsu Sheng, China*

[89]*AIM, CEA, CNRS, Université Paris Diderot, Sorbonne Paris Cité, Université Paris-Saclay, F-91191 Gif-sur-Yvette, France*

[90]*Astrophysics, Department of Physics, University of Oxford, Keble Road, Oxford OX1 3RH, UK*

[91]*Department of Physics, The George Washington University, 725 21st Street NW, Washington, DC 20052, USA*

[92]*Astronomy, Physics, and Statistics Institute of Sciences (APSIS), The George Washington Uni-*

versity, Washington, DC 20052, USA

[93]*Inter-University Institute for Data-Intensive Astronomy, Department of Astronomy, University of Cape Town, Private Bag X3, Rondebosch 7701, South Africa*

[94]*GEPI, Observatoire de Paris, PSL University, CNRS, 5 Place Jules Janssen, 92190 Meudon, France*

[95]*Depto. de Física Teórica, Universidad de Zaragoza, E-50019, Zaragoza, Spain*

[96]*National Radio Astronomy Observatory, 1003 Lopezville Road, Socorro, NM 87801, USA*

[97]*Caltech, 1200 California Blvd., Pasadena, CA 91106, USA*

[98]*Osservatorio Astronomico 'S. Di Giacomo' - AstroCampania, I-80051, Agerola (NA), Italy*

[99]*INAF - Astronomical Observatory of Naples, I-23807 Naples (NA), Italy*

[100]*Astrophysics Research Centre, School of Mathematics and Physics, Queens University Belfast, Belfast BT7 1NN, UK*

[101]*Benoziyo Center for Astrophysics, Weizmann Institute of Science, 76100 Rehovot, Israel*

[102]*Tuorla Observatory, Department of Physics and Astronomy, University of Turku, 20014 Turku, Finland*

[103]*School of Physics & Astronomy, Cardiff University, Queens Buildings, The Parade, 25 Cardiff, CF24 3AA, UK*

[104]*School of Physics, Trinity College Dublin, Dublin 2, Ireland*

[105]*INAF - Osservatorio di Astrofisica e Scienza dello Spazio, via Piero Gobetti 93/3, 40129 Bologna, Italy*

[106]*Astrophysics Science Division, NASA Goddard Space Flight Center, 8800 Greenbelt Rd,*

Greenbelt, MD 20771, USA

[107] *Scuola Universitaria Superiore IUSS Pavia, Piazza della Vittoria 15, 27100 Pavia, Italy*

[108] *INAF - IASF Milano, Via E. Bassini 15, 20133 Milano, Italy*

[109] *Istituto Nazionale di Fisica Nucleare, Sezione di Pavia, Via Bassi 6, 27100 Pavia, Italy*

[110] *Department of Astrophysics, Institute of Mathematics, Astrophysics and Particle Physics (IMAPP), Radboud University Nijmegen, Nijmegen, the Netherlands*

[111] *Space Telescope Science Institute, 3700 San Martin Drive, Baltimore, MD 21218, USA*

[112] *Cosmic Dawn Center (DAWN)*

[113] *Niels Bohr Institute, Copenhagen University, Vibenshuset, Lyngbyvej 2, DK-2100, Copenhagen*

[114] *Centre for Astrophysics and Cosmology, Science Institute, University of Iceland, Dunhagi 5, 107 Reykjavík, Iceland*

[115] *Departamento de Astrofisica, Universidad de La Laguna, Tenerife, Spain*

[116] *Physics and Astronomy Department, University of Southampton, Southampton, UK*

[117] *Warsaw University Astronomical Observatory, Al. Ujazdowskie 4, PL-00- 478 Warszawa, Poland*

[118] *Institute for Astronomy, University of Edinburgh, Royal Observatory, Blackford Hill, EH9 3HJ, UK*

[119] *Birmingham Institute for Gravitational Wave Astronomy and School of Physics and Astronomy, University of Birmingham, Birmingham B15 2TT, UK*

[120] *Dipartimento di Scienze Fisiche, Universit degli studi di Napoli Federico II, Via Cinthia, Edificio N, 80126 Napoli, Italy*

[121]*INFN, Sezione di Napoli, Complesso Universitario di Monte S. Angelo, Via Cinthia, Edificio N, 80126 Napoli, Italy*

[122]*DTU Space, National Space Institute, Technical University of Denmark, Elektrovej 327, 2800 Kongens Lyngby, Denmark*

[123]*CAS Key Laboratory of Space Astronomy and Technology, National Astronomical Observatories, Chinese Academy of Sciences, Beijing 100012, China*

[124]*Anton Pannekoek Institute for Astronomy, University of Amsterdam, Science Park 904, 1098 XH Amsterdam, The Netherlands*

[125]*International Center for Relativistic Astrophysics Network (ICRANet), Piazzale della Repubblica 10, I-65122, Pescara, Italy*

Long-duration gamma-ray bursts (GRBs) originate from ultra-relativistic jets launched from the collapsing cores of dying massive stars. They are characterised by an initial phase of bright (typical observed fluxes $10^{-7} - 10^{-3}$ erg cm^{-2} s^{-1}) and highly variable ($\ll$1 second) radiation in the 0.1-1 MeV band that is likely produced within the jet and lasts from milliseconds to minutes, known as the prompt emission. Following the prompt emission, the interaction of the ultra-relativistic jet with the external medium generates external shocks, responsible for the so-called afterglow emission, which lasts from days to months, and occurs over a broad energy range, including the soft X-ray, optical and radio bands[1–5]. The origin of the afterglow emission is explained and modeled as synchrotron radiation from the shock accelerated electrons[6–9]. Recently, the Major Atmospheric Gamma Imaging Cherenkov (MAGIC) telescopes revealed for the first time intense, long-lasting emission between 0.2 and 1 TeV from GRB 190114C[10]. Here we present the results of our multi-frequency observational campaign, and study the evolution in time of the GRB emission across 17 orders of magnitude in energy, from 5×10^{-6} up to 10^{12} eV. We find that the broadband spectral energy distribution is double-peaked, with the TeV emission constituting a distinct spectral component that has power comparable to the synchrotron component. This component is associated with the afterglow, and is satisfactorily explained by inverse Compton upscattering of synchrotron photons by high-energy electrons. The inclusion of TeV observations in GRB studies gives additional information to pinpoint the conditions of the source.

We find that the inferred conditions required to explain the presence of the TeV component and its temporal behaviour are not atypical. Our results support the possibility that inverse

Compton emission is commonly produced in GRBs.

On 14 January 2019, following an alert from the Neil Gehrels Swift Observatory (hereafter *Swift*) and the *Fermi* satellites, MAGIC observed and detected radiation up to at least 1 TeV from GRB 190114C. **Before the MAGIC detection, GRBs have been detected only at much lower energies,** $\lesssim 100$ **GeV. A hint for the presence of** $\sim$**TeV emission (**$\gtrsim 650$ **GeV) was found by the Milagrito experiment from observations of GRB 970417A[11]. GeV emission has been detected first by *CGRO*/EGRET in a handful of cases, and more recently by *AGILE*/GRID and *Fermi*/LAT (see [12] for a recent review).**

Detection of TeV radiation opens a new window in the electromagnetic spectrum for the study of GRBs[10]. Its announcement[13] triggered an extensive campaign of follow-up observations. Owing to the relatively low redshift $z = 0.4245 \pm 0.0005$ (see Methods) of the GRB (corresponding to a luminosity distance of $\sim$ 2.3 Gpc) a comprehensive set of multi-wavelength data could be collected. We present observations gathered from instruments onboard six satellites and 15 ground telescopes (radio, submm and NIR/optical/UV and very high energy gamma-rays; see Methods) for the first ten days after the burst. The frequency range covered by these observations spans more than 17 orders of magnitude, from 1 to $\sim 2 \times 10^{17}$ GHz, the most extensive to date for a GRB. The light curves of GRB 190114C at different frequencies are shown in Fig. 1.

The prompt emission of GRB 190114C was simultaneously observed by several space missions (see Methods), covering the spectral range from 8 keV to $\sim$ 100 GeV. The prompt light curve shows a complex temporal structure, with several emission peaks (Methods; Extended Data Fig. 1),

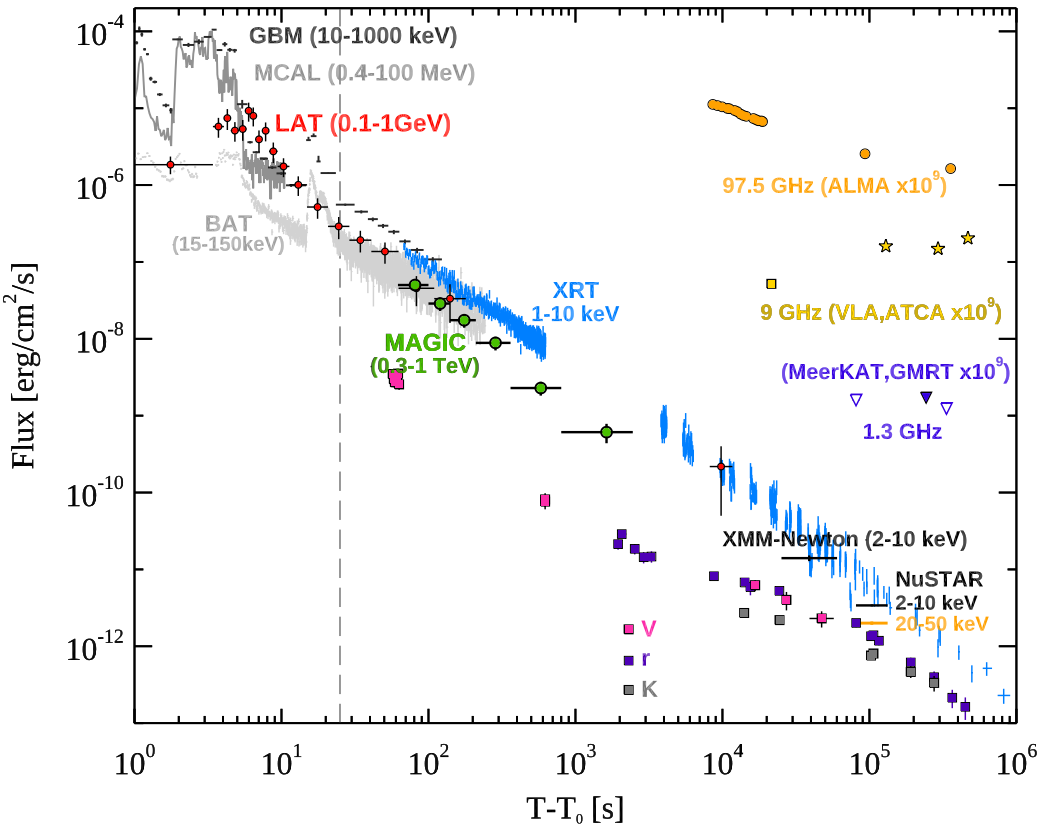

Figure 1: **Multi-wavelength light curves of GRB 190114C.** Energy flux at different wavelengths, from radio to gamma-rays, versus time since the BAT trigger time $T_0 = 20{:}57{:}03.19$ UT on 14 January 2019. The light curve for the energy range 0.3-1 TeV (green circles) is compared with light curves at lower frequencies. Those for VLA (yellow square), ATCA (yellow stars), ALMA (orange circles), GMRT (purple filled triangle), and MeerKAT (purple empty triangles) have been multiplied by 10^9 for clarity. The vertical dashed line marks approximately the end of the prompt emission phase, identified with the end of the last flaring episode. For the data points, vertical bars show the 1-σ errors on the flux, while horizontal bars represent the duration of the observation.

with total duration ~ 25 s (see dashed line in Fig. 1) and total radiated energy $E_{\gamma,\mathrm{iso}}$ = (2.5 $\pm$ 0.1) $\times 10^{53}$ ergs [14] (isotropic equivalent in the energy range 1-10000 keV). During the time of inter-burst quiescence at $t \sim [5-15]$ seconds and after the end of the last prompt pulse at $t \gtrsim 25$ s, the flux decays smoothly, following a power law in time $F \propto t^{\alpha}$, with $\alpha_{10-1000\mathrm{keV}} = -1.10 \pm 0.01$ [14]. The temporal and spectral characteristics of this smoothly varying component support an interpretation in terms of afterglow synchrotron radiation[14,15], making this one of the few clear cases of afterglow emission detected in the band $10 - 10^4$ keV during the prompt emission phase. The onset of the afterglow component is then estimated to occur around $t \sim 5 - 10$ s [14,15], implying an initial bulk Lorentz factor between 300 and 700 (Methods).

After about one minute from the start of the prompt emission, two additional high-energy telescopes began observations: MAGIC and the XRT, onboard *Swift*. The XRT and MAGIC light curves (1-10 keV, blue data points in Fig. 1, and 0.3-1 TeV, green data points, respectively) decay with time as a power law, and display the following decay rates: $\alpha_{\mathrm{X}} \sim -1.36 \pm 0.02$ and $\alpha_{\mathrm{TeV}} \sim -1.51 \pm 0.04$. The 0.3-1 TeV light curve shown in Fig. 1 was obtained after correcting for attenuation by the extragalactic background light (EBL)[10]. The TeV-band emission is observable until $\sim$40 minutes, which is much longer than the nominal duration of the prompt emission phase. The NIR-optical light curves (square symbols) show a more complex behaviour. Initially, a fast decay is seen, where the emission is most likely dominated by the reverse shock component[16]. This is followed by a shallower decay, and subsequently a faster decay at $\sim 10^5$ s. The latter behaviour is not atypical, **but is usually seen at earlier times and** indicates that the characteristic synchrotron frequency ν_{m} is crossing the optical band **(Extended Data Fig. 11)**. **The relatively**

late time where the break appears in GRB 190114C would then imply a very large value of $\nu_{\rm m}$, placing it in the X-ray band at $\sim 10^2$ s.. The millimeter light curves (orange symbols) also show an initial fast decay where the emission is dominated by the reverse shock, followed by emission at late times with nearly constant flux (Extended Data Fig. 10).

The spectral energy distributions (SEDs) of the radiation detected by MAGIC are shown in Fig. 2, where the whole duration of the emission detected by MAGIC is divided into five time intervals. For the first two time intervals, observations in the GeV and X-ray bands are also available. During the first time interval (68-110 s, blue data points and blue confidence regions), *Swift*/XRT-BAT and *Fermi*/GBM data show that the afterglow synchrotron component is peaking in the X-ray band. At higher energies, up to $\lesssim$ GeV, the SED is a decreasing function of energy, as supported by the *Fermi*/LAT flux between 0.1 and 0.4 GeV (see Methods). On the other hand, at even higher energies, the MAGIC flux above 0.2 TeV implies a spectral hardening. This evidence is independent from the EBL model adopted to correct for the attenuation (Methods). This demonstrates that the newly discovered TeV radiation is not a simple extension of the known afterglow synchrotron emission, but rather a separate spectral component that has not been clearly seen before.

The extended duration and the smooth, power-law temporal decay of the radiation detected by MAGIC (see green data points in Fig. 1) suggest an intimate connection between the TeV emission and the broadband afterglow emission. The most natural candidate is synchrotron self-Compton (SSC) radiation in the external forward shock: the same population of relativistic electrons responsible for the afterglow synchrotron emission Compton upscatters the synchrotron pho-

tons, leading to a second spectral component that peaks at higher energies. TeV afterglow emission can also be produced by hadronic processes such as synchrotron radiation by protons accelerated to ultra-high energies in the forward shock[17–19]. However, due to their typically low efficiency of radiation[5], reproducing the luminous TeV emission as observed here by such processes would imply unrealistically large power in accelerated protons[10]. TeV photons can also be produced via the SSC mechanism in internal shock synchrotron models of the prompt emission. However, numerical modeling (Methods) shows that prompt SSC radiation can account at most for a limited fraction ($\lesssim 20\%$) of the observed TeV flux, and only at early times ($t \lesssim 100\,\mathrm{s}$). Henceforth, we focus on the SSC process in the afterglow.

SSC emission has been predicted for GRB afterglows[9,12,18,20–27]. However, **its** quantitative significance for the latter was uncertain, as the SSC luminosity and spectral properties depend strongly on poorly constrained physical conditions in the emission region (e.g., the magnetic field strength). The detection of the TeV component in GRB 190114C and the availability of broad band observations offer the opportunity to investigate the relevant physics at a deeper level. **A hint of SSC component might have been detected in very bright GRBs, such as GRB 130427A. The GRB 130427A extended emission with photons up to $\sim 100\,$GeV is hardly modeled by synchrotron processes, suggesting a different origin of the photons[28–30].**

With this aim, we model the full data set (from radio band to TeV energies, for the first week after the explosion) as synchrotron plus SSC radiation, within the framework of the theory of afterglow emission from external reverse-forward shocks. The detailed modeling of the broadband

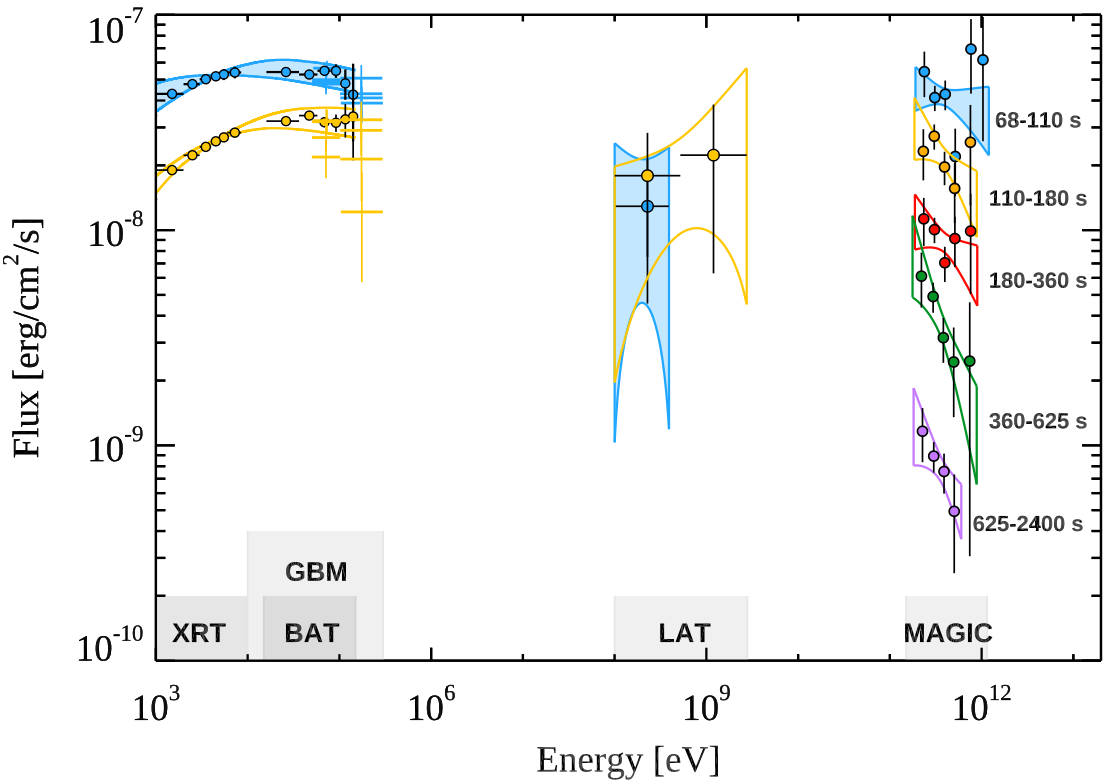

Figure 2: **Broadband spectra in the time interval 68-2400 s**. Five time intervals are considered: 68-110 s (blue), 110-180 s (yellow), 180-360 s (red), 360-625 s (green), 625-2400 s (purple). MAGIC data points have been corrected for attenuation caused by the Extragalactic Background Light. Data from other instruments are shown for the first two time-intervals: *Swift*/XRT, *Swift*/BAT, *Fermi*/GBM, and *Fermi*/LAT. For each time interval, LAT contour regions are shown limiting the energy range to the range where photons are detected. MAGIC and LAT contour regions are drawn from the 1-σ error of their best-fit power law functions. For *Swift* data, the regions show the 90% confidence contours for the joint fit XRT-BAT obtained fitting to the data a smoothly broken power law. Filled regions are used for the first time interval (68-110 s, blue color).

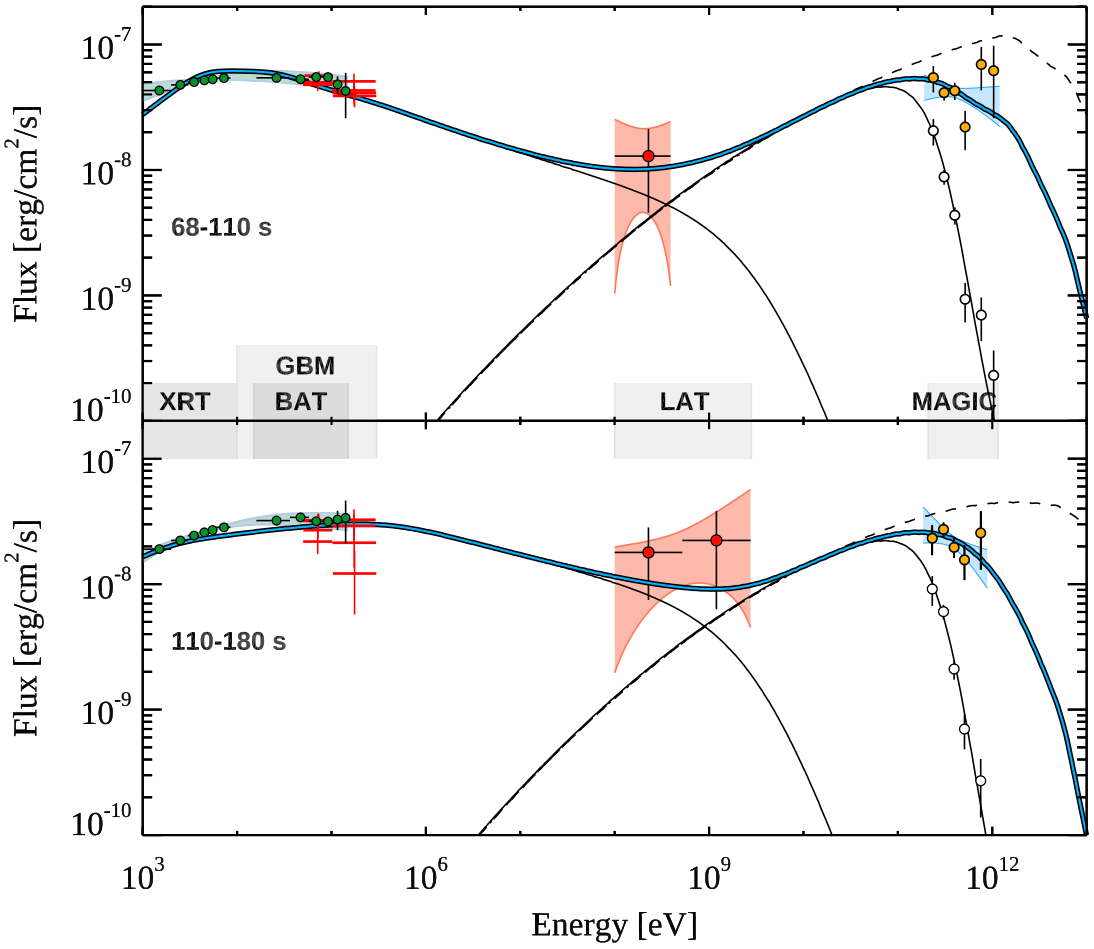

Figure 3: **Modeling of the broadband spectra in the time intervals 68-110 s and 110-180 s.** Thick blue curve: modeling of the broadband data in the synchrotron and SSC afterglow scenario. Thin solid lines: synchrotron and SSC (observed spectrum) components; dashed lines: SSC if internal γ-γ opacity is neglected. For the adopted parameters, see the Text. Empty circles show the observed MAGIC spectrum, i.e. not corrected by attenuation caused by the Extragalactic Background Light. Contour regions and data points as in Fig. 2.

emission and its evolution with time is presented in Section Methods. We discuss here the implications for the early time ($t < 2400$ s), high energy (> 1 keV) emission. Information inferred from late time optical data, allows to identify the peak of the synchrotron component visible in the X-ray band at ~ 100 s as the characteristic frequency $\nu_{\rm m}$. The soft spectra (photon index $\Gamma_{\rm TeV} < -2$) in the 0.2-1 TeV energy range (see Extended Data Table 1) constrain the peak of the SSC component to be below this energy range. The relatively small ratio between the spectral peak energies of the SSC ($E_{\rm p}^{\rm SSC} \lesssim 200$ GeV) and synchrotron ($E_{\rm p}^{\rm syn} \sim 10$ keV) components implies a relatively low value for the minimum Lorentz factor of the electrons ($\gamma_{\rm m} \sim 2 \times 10^3$). This value is inconsistent with the observation of the synchrotron peak at $\gtrsim$keV energies, leading to the conclusion that Klein-Nishina (KN) scattering effects and/or internal opacity caused by γ-γ pair production have a substantial impact on the spectra. We find that in order to explain the soft spectrum detected by MAGIC, it is necessary to invoke KN-regime scattering for the electrons radiating at the spectral peak as well as internal γ-γ absorption.

While both effects tend to become less important with time, the spectral index in the 0.2-1 TeV band remains constant in time (or possibly evolves to softer values; Extended Data Table 1). This implies that the SSC peak energy is moving to lower energies and crossing the MAGIC energy band. This places robust constraints on the minimum energy of the electrons: $\gamma_{\rm m} = (1-5) \times 10^4$. The energy at which attenuation by internal pair production becomes important indicates that the bulk Lorentz factor is $\sim$120-140 at 100 s.

An example of the theoretical modeling in this scenario is shown in Fig. 3 (blue solid curve,

see Methods for details). The dashed line shows the SSC spectrum when internal absorption is neglected. The thin solid line shows the model spectrum including EBL attenuation, in comparison to MAGIC observations (empty circles).

We find that acceptable models of the broadband SED can be obtained if the conditions at the source are the following: the initial kinetic energy of the blastwave is $E_{\rm k} \gtrsim 2 \times 10^{53}$ erg (isotropic-equivalent). At least a fraction $\xi_{\rm e} \sim 0.1$ in number of the electrons swept up from the external medium are efficiently injected into the acceleration process, and carry a fraction $\epsilon_{\rm e} \sim 0.05 - 0.15$ of the energy dissipated at the shock. The acceleration mechanism produces an electron population characterized by a non-thermal energy distribution, described by a power law with index $p \sim 2.4 - 2.5$, injection Lorentz factor $\gamma_{\rm m} = 10^4 - 5 \times 10^4$ and maximum Lorentz factor $\gamma_{e,\rm max} \sim 10^7$ (at $\sim 100\,$s). The magnetic field behind the shock conveys a fraction $\epsilon_{\rm B} \sim (0.05 - 1) \times 10^{-3}$ of the dissipated energy. At $t \sim 100\,$s, corresponding to $R \sim (6 - 8) \times 10^{16}\,$cm, the density of the external medium is $n > 1\,{\rm cm}^{-3}$, and the magnetic field strength is $B \sim 0.1 - 10\,$Gauss. The latter implies that the magnetic field was efficiently amplified from values of a few μGauss that are typical of the unshocked ambient medium, due to plasma instabilities or other mechanisms[5].

The blastwave energy inferred from the modeling is comparable to the amount of energy released in the form of radiation during the prompt phase. The prompt emission mechanism must then have dissipated and radiated no more than half of the initial jet energy, leaving the other half available for the afterglow phase. The modeling of the broadband data also allows us to infer how the total energy is shared between the synchrotron and the SSC components. SSC would be

2-3 times more energetic than synchrotron if internal γ-γ absorption is neglected, but the latter substantially affects SSC such that the resultant power in the two components are comparable. We estimate that the energy in the synchrotron and SSC component are $\sim 6.5 \times 10^{51}$ erg and $\sim 1.0 \times 10^{52}$ erg respectively in the time interval 68-110 s, and $\sim 9.6 \times 10^{51}$ erg and $\sim 1.6 \times 10^{52}$ erg respectively in the time interval 110-180 s. Thus, previous studies of GRBs may have been missing a significant fraction of the energy **emitted during the afterglow phase** that is essential for **its** understanding.

Finally, we note that the values of the afterglow parameters inferred from the modeling fall within the range of typical values inferred from broadband (radio-to-GeV) afterglow studies. This points to the possibility that SSC emission in GRBs may be a relatively common process that does not require special conditions to be produced with power similar to synchrotron radiation. **Not surprisingly, the inferred parameters imply that the energy density of the radiation field is much larger than the energy density of the magnetic field[18,20], i.e.** $\epsilon_{\rm e} > \epsilon_{\rm B}$**).** The SSC component may then be detectable in other relatively energetic GRBs **(and might have been already detected in past events [28–30])**, as long as the redshift is low enough to avoid severe attenuation by the EBL.

Methods

Prompt emission observations On 14 January 2019, the prompt emission from GRB 190114C triggered several space instruments, including *Fermi*/GBM[31], *Fermi*/LAT[32], *Swift*/BAT[33], Super-AGILE[34], *AGILE*/MCAL[34], *KONUS*/Wind[35], *INTEGRAL*/SPI-ACS[36], and *Insight*/HXMT[37]. The prompt emission light curves from *AGILE*, *Fermi*, and *Swift* are shown in Fig. 1 and in Extended Data Fig. 1, **where the trigger time T_0 (here and elsewhere) refers to the BAT trigger time (20:57:03.19 UT).** The prompt emission lasts approximately for 25 s, where the last flaring emission episode ends. Nominally, the T_{90}, i.e. the time interval during which a fraction between 5% and 95% of the total emission is observed, is much longer (> 100 s, depending on the instrument[14]), but is clearly contaminated by the afterglow component (Fig. 1) and does not provide a good measure of the actual duration of the prompt emission. A more detailed study of the prompt emission phase is reported in [14].

AGILE (The Astrorivelatore Gamma ad Immagini LEggero [38]) could observe GRB 190114C until T_0+330 s, before it became occulted by the Earth. GRB 190114C triggered the Mini-CALorimeter (MCAL) from T0$-$0.95 s to T0$+$10.95 s. The MCAL light flux curve in Fig. 1 has been produced using two different spectral models. From $T_0-0.95$ s to $T_0+1.8$ s, the spectrum is fitted by a power law with photon index $\Gamma_{\rm ph}$ = -1.97$^{+0.47}_{-0.70}$ ($dN/dE \propto E^{\Gamma_{\rm ph}}$) From $T_0+1.8$ s to $T_0 + 5.5$ s the best fit model is a broken power law with $\Gamma_{\rm ph,1} = -1.87^{+0.54}_{-0.19}$, $\Gamma_{\rm ph,2} = -2.63^{+0.07}_{-0.07}$, and break energy $E_{\rm b}$ =756^{+137}_{-159} keV. The total fluence in the 0.4$-$100 MeV energy range is $F = 1.75\times10^{-4}$ erg cm^{-2}. The Super-AGILE detector also detected the burst, but the large off-axis angle prevented any X-ray imaging of the burst, as well as spectral analysis. Panels **a**, **d**, and **e**

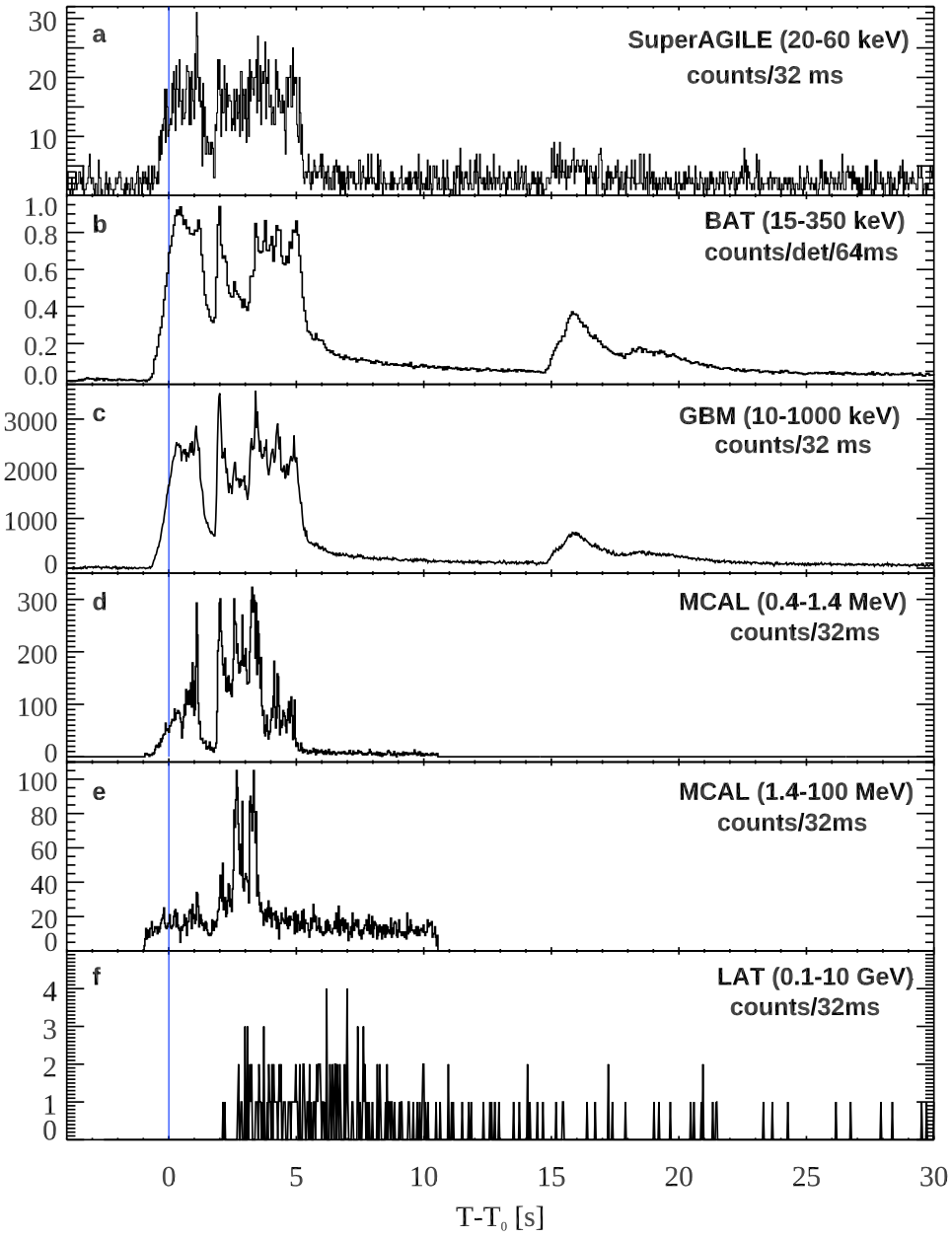

Extended Data Figure 1: **Prompt emission light curves for different detectors.** The different panels show light curves for: **a**, SuperAGILE (20-60 keV); **b**, *Swift*/BAT (15-150 keV); **c**, *Fermi*/GBM (10-1000 keV); **d**, *AGILE*/MCAL (0.4-1.4 MeV); **e**, *AGILE*/MCAL (1.4-100 MeV); **f**, *Fermi*/LAT (0.1-10 GeV). The light curve of *AGILE*/MCAL is split into two bands to show the energy dependence of the first peak. Error bars show the 1-σ statistical errors.

in Extended Data Fig. 1 show the GRB 190114C light curves acquired by the Super-AGILE detector ($20-60$ keV) and by the MCAL detector in the low- ($0.4-1.4$ MeV) and high-energy ($1.4-100$ MeV) bands.

***Fermi*/GBM** At the time of the MAGIC observations there are indications that some of the detectors are partially blocked by structure on the *Fermi* Spacecraft that is not modeled in the GBM detectors' response. This affects the low-energy part of the spectrum [39]. For this reason, out of caution we elected to exclude the energy channels below 50 keV. The spectra detected by the *Fermi*-Gamma-ray Burst Monitor (GBM)[40] during the T_0+68 s to T_0+110 s and T_0+110 s to T_0+180 s intervals are best described by a power law model with photon index $\Gamma_{\rm ph} = -2.10 \pm 0.08$ and $\Gamma_{\rm ph} = -2.05 \pm 0.10$ respectively (Fig. 2 and Fig. 3). The 10-1000 keV light curve in Extended Data Fig. 1 (panel **c**) was constructed by summing photon counts for the bright NaI detectors.

***Swift*/BAT** The $15-350$ keV mask-weighted light curve of the Burst Alert Telescope (BAT [41]) shows a multi-peaked structure that starts at T_0-7 s (Extended Data Fig. 1, panel **b**). The $68-110$ s and $110-180$ s spectra shown in Figs. 2 and 3 were derived from joint XRT-BAT fit. The best-fitting parameters for the whole interval ($68-180$ s) are: column density $N_{\rm H} = (7.53^{+0.74}_{-1.74}) \times 10^{22}$ cm^{-2} at $z = 0.42$, in addition to the galactic value of 7.5×10^{19} cm^{-2}, low-energy photon index $\Gamma_{\rm ph,1} = -1.21^{+0.40}_{-1.26}$, high-energy spectral index $\Gamma_{\rm ph,2} = -2.19^{+0.39}_{-0.19}$, peak energy $E_{\rm pk} > 14.5$ keV. Errors are given at 90% confidence level.

***Fermi*/LAT** The *Fermi* Large Area Telescope (LAT)[42] detected a gamma-ray counterpart since the prompt phase[43]. The burst left the LAT FoV at T_0+150 s and remained outside the LAT field of

view until T_0+8600 s. The count light curve in the energy range 0.1-10 GeV is shown in Extended Data Fig. 1 (panel **f**). The LAT spectra in the time bins 68–110 s and 110–180 s (Figs. 2 and 3) are described by a power law with pivot energies of, respectively, 200 MeV and 500 MeV, photon indices $\Gamma_{\rm ph}(68-110) = -2.02 \pm 0.95$ and $\Gamma_{\rm ph}(110-180) = -1.69 \pm 0.42$, and corresponding normalisations of $N_{0,68-110} = (2.02 \pm 1.31) \times 10^{-7}$ ph MeV^{-1}cm^{-2} s and $N_{0,110-180} = (4.48 \pm 2.10) \times 10^{-8}$ ph MeV^{-1}cm^{-2} s. In each time-interval, the analysis has been performed limited to the energy range where photons have been detected. The LAT light curve integrated in the energy range 0.1-1 GeV is shown in Fig. 1.

MAGIC We used the Major Atmospheric Gamma Imaging Cherenkov (MAGIC) standard software [44] and followed the steps optimised for the data taking under moderate moon illumination[45] to analyse the data. The spectral fitting is performed by a forward-folding method assuming a simple power law as for an intrinsic spectrum taking into account of the Extragalactic Background Light (EBL) effect using the model of Domínguez et al.[46]. Extended Data Table 1 shows the fitting results for various time bins (the pivot energy is chosen to minimise the correlation between normalisation and photon index parameters). The data points shown in both Fig. 2 and 3 are obtained from the observed excess rates in estimated energy whose fluxes are evaluated in true energy using effective time and a spill-over corrected effective area obtained as a resultant of the best fit.

The time resolved analysis hints to a possible spectral evolution from hard to soft values. Although we can not exclude that the photon indexes are compatible with a constant value of ~ -2.5 up to 2400 s. The signal and background in the considered time bins are both in the low-count Poisson regime. Therefore, the correct treatment of the MAGIC data provided here includes

Time bin [seconds after T_0]	Normalisation [$\mathrm{TeV}^{-1}\,\mathrm{cm}^{-2}\,\mathrm{s}^{-1}$]	Photon index	Pivot energy [GeV]
62 - 90	$1.95^{+0.21}_{-0.20} \cdot 10^{-7}$	$-2.17^{+0.34}_{-0.36}$	395.5
68 - 180	$1.10^{+0.09}_{-0.08} \cdot 10^{-7}$	$-2.27^{+0.24}_{-0.25}$	404.7
180 - 625	$2.26^{+0.21}_{-0.20} \cdot 10^{-8}$	$-2.56^{+0.27}_{-0.29}$	395.5
68 - 110	$1.74^{+0.16}_{-0.15} \cdot 10^{-7}$	$-2.16^{+0.29}_{-0.31}$	386.5
110 - 180	$8.59^{+0.95}_{-0.91} \cdot 10^{-8}$	$-2.51^{+0.37}_{-0.41}$	395.5
180 - 360	$3.50^{+0.38}_{-0.36} \cdot 10^{-8}$	$-2.36^{+0.34}_{-0.37}$	395.5
360 - 625	$1.65^{+0.23}_{-0.23} \cdot 10^{-8}$	$-3.16^{+0.48}_{-0.54}$	369.1
625 - 2400	$3.52^{+0.47}_{-0.47} \cdot 10^{-9}$	$-2.80^{+0.48}_{-0.54}$	369.1
62 - 2400 (Nominal MC)	$1.07^{+0.08}_{-0.07} \cdot 10^{-8}$	$-2.51^{+0.20}_{-0.21}$	423.8
62 - 2400 (Light scale +15% MC)	$7.95^{+0.58}_{-0.56} \cdot 10^{-9}$	$-2.91^{+0.23}_{-0.25}$	369.1
62 - 2400 (Light scale -15% MC)	$1.34^{+0.09}_{-0.09} \cdot 10^{-8}$	$-2.07^{+0.18}_{-0.19}$	509.5

Extended Data Table 1: **MAGIC spectral fit parameters for GRB 190114C.** For each time bin, columns represent a) start time and end time of the bin; b) normalisation of the EBL-corrected differential flux at the pivot energy with statistical errors; c) photon indices with statistical errors; d) pivot energy of the fit (fixed).

along with the use of the Poisson statistic also the systematic errors. To estimate the main source of systematic error caused by our imperfect knowledge of the absolute instrument calibration and the total atmospheric transmission we vary the light-scale in our Monte Carlo (MC) simulation as suggested in previous studies[44]. The result is reported in the last two lines of Extended Data Table 1 and in Extended Data Fig. 2.

The systematic effects deriving from the choice of one particular EBL model were also studied. The analysis performed to obtain the time integrated spectrum was repeated employing other three models[47–49] to deconvolve the effect of the EBL from the spectral data. The contribution to the systematic error on the photon index caused by the uncertainty on the EBL model is $\sigma_\alpha = ^{+0.10}_{-0.13}$ which is smaller than the statistical error only (1 standard deviation) as already seen in a previous work[10]. On the other hand the contribution to the systematic error on the normalisation, due to choice of the EBL model, is only partially at the same level of the statistical error (1 standard deviation) $\sigma_N = ^{+0.30}_{-0.08} \times 10^{-8}$. The chosen EBL model returns a lower normalisation with respect to two of the other models and very close to the rest [47].

The MAGIC energy flux light curve that is presented in Fig. 1 was obtained by integrating the best fit spectral model of each time bin from 0.3 to 1 TeV, in the same manner as a previous publication[10]. The value of the fitted time constant reported here differs less than two standard deviation from the one previously reported[10]. The difference is due to the poor constraints on the spectral fit parameters of the last time bin, which influences the light curve fit.

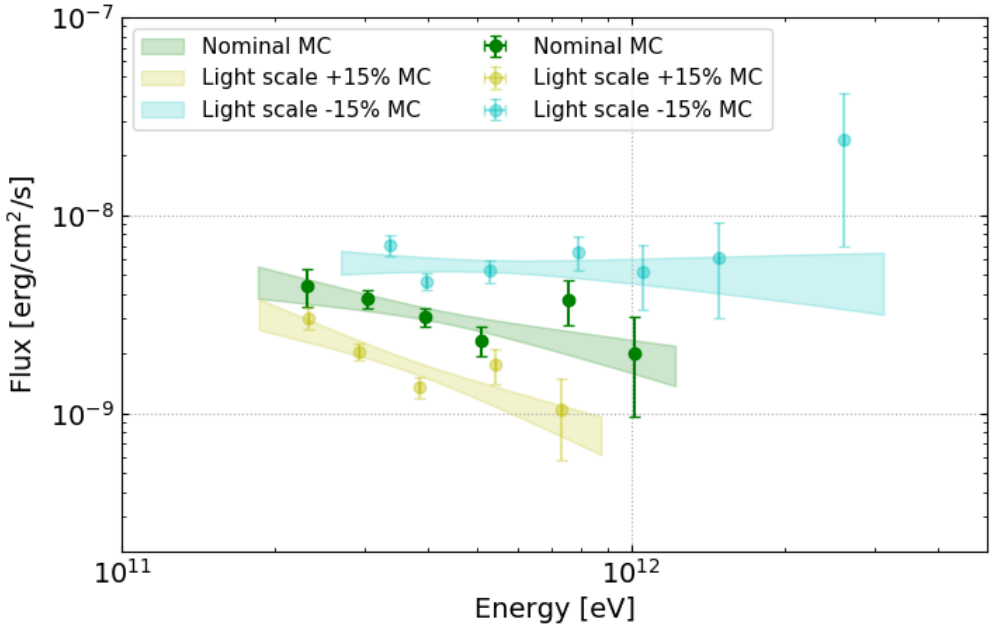

Extended Data Figure 2: **MAGIC time integrated spectral energy distributions in the time interval 62-2400 s after T_0.** The green (yellow, blue) points and band show the result with the nominal (+15%, -15%) light scale MC, defining the limits of the systematic uncertainties.

X-ray afterglow observations

***Swift*/XRT** The *Swift* X-Ray Telescope (XRT) started observing 68 s after T_0. The source light curve[50] was taken from the *Swift*/XRT light curve repository [51] and converted into 1-10 keV flux (Fig. 1) through dedicated spectral fits. The combined spectral fit XRT+BAT in Figs. 2 and 3 has been described above.

XMM-Newton* and *NuSTAR The *XMM-Newton* X-ray Observatory and the the Nuclear Spectroscopic Telescope Array (*NuSTAR*) started observing GRB 190114C under DDT ToOs 7.5 hours and 22.5 hrs (respectively) after the burst. The *XMM-Newton* and NuSTAR absorption-corrected fluxes (see Fig. 1) were derived by fitting the spectrum with XSPEC adopting the same power law model, with absorption in our Galaxy and at the redshift of the burst.

NIR, Optical and UV afterglow observations

Light curves from the different instruments presented in this section are shown in Extended Data Fig. 3.

GROND The Gamma-ray Burst Optical/Near-infrared Detector (GROND[52]) started observations 3.8 hours after the GRB trigger, and the follow-up continued until January 29, 2019. Image reduction and photometry were carried out with standard IRAF tasks [53], as described in [54,55]. $JHK_{\rm s}$ photometry was converted to AB magnitudes to have a common flux system. Final photometry is given in Extended Data Table 2.

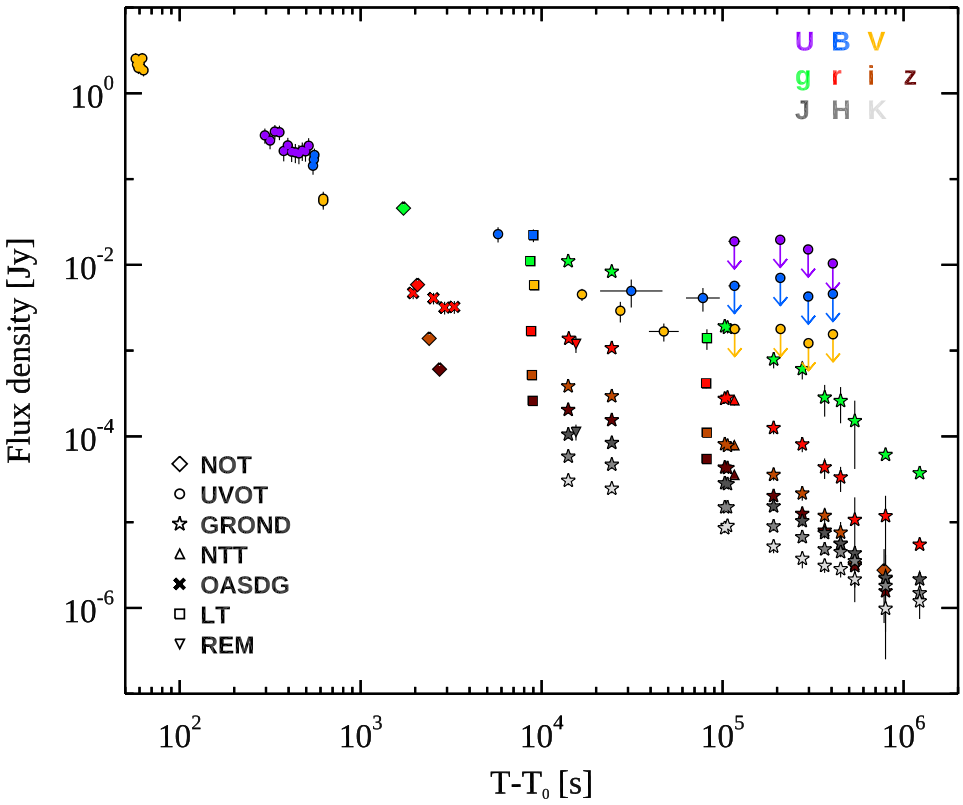

Extended Data Figure 3: **NIR/Optical/UV observations GRB 190114C.** Energy flux at different frequencies, as a function of the time since the initial burst T_0. The flux has been corrected for extinction in the host and in our Galaxy. The contribution of the host galaxy and its companion has been subtracted. Fluxes have been rescaled (except for the r filter). The change in decay rate at $\sim 3 \times 10^3$ s is caused by the transition from the fast cooling to the slow cooling regime.

GTC The BOOTES-2 ultra-wide field camera [56], took an image at the GRB 190114C location, starting at 20:57:18 UT (30 s exposure time) (see Extended Data Fig. 4). The Gran Canarias Telescope (GTC) equipped with the OSIRIS spectrograph[57] started observations 2.6 hr post-burst. The grisms R1000B and R2500I were used covering the wavelength range 3,700-10,000 Å (600 s exposure times for each grism). The GTC detects a highly extinguished continuum, as well as CaII H and K lines in absorption, and [OII], H_β, and [OIII] in emission (see Extended Data Fig. 5), all roughly at the same redshift $z = 0.4245 \pm 0.0005$ [58]. Comparing the derived rest-frame equivalent widths (EWs) with the work by [59], GRB 190114C clearly shows higher than average, but not unprecedented, values.

HST The *Hubble Space Telescope* (*HST*) imaged the afterglow and host galaxy of GRB 190114C on 11 February and 12 March 2019. HST observations clearly reveal that the host galaxy is spiral (Extended Data Fig. 6). A direct subtraction of the epochs of F850LP observations yields a faint residual close to the nucleus of the host (Extended Data Fig. 7). From the position of the residual we estimate that the burst originated within 250 pc of the host galaxy nucleus.

LT The robotic 2-m Liverpool Telescope (LT[60]) slewed to the afterglow location at UTC 2019-01-14.974 and on the second night, from UTC 2019-01-15.814 and acquired images in B, g, V, r, i and z bands (45 s exposure each in the first night and 60 s in the second). Aperture photometry of the afterglow was performed using a custom IDL script with a fixed aperture radius of 1.5″. Photometric calibration was performed relative to stars from the Pan-STARRS1 catalogue[61].

$T_{\rm GROND}$	AB magnitude						
(s)	g'	r'	i'	z'	J	H	K_s
14029.94 ± 335.28	19.21 ± 0.03	18.46 ± 0.03	17.78 ± 0.03	17.33 ± 0.03	16.78 ± 0.05	16.30 ± 0.05	16.03 ± 0.07
24402.00 ± 345.66	19.50 ± 0.04	18.72 ± 0.03	18.05 ± 0.03	17.61 ± 0.03	17.02 ± 0.05	16.53 ± 0.05	16.26 ± 0.08
102697.17 ± 524.01	20.83 ± 0.06	20.00 ± 0.04	19.30 ± 0.04	18.87 ± 0.03	18.15 ± 0.05	17.75 ± 0.06	17.40 ± 0.09
106405.63 ± 519.87	20.86 ± 0.05	19.98 ± 0.03	19.34 ± 0.03	18.88 ± 0.03	18.17 ± 0.06	17.75 ± 0.06	17.34 ± 0.09
191466.77 ± 751.37	21.43 ± 0.07	20.61 ± 0.03	19.97 ± 0.03	19.52 ± 0.03	18.77 ± 0.06	18.28 ± 0.06	17.92 ± 0.14
275594.19 ± 747.59	21.57 ± 0.07	20.88 ± 0.04	20.31 ± 0.04	19.87 ± 0.04	19.14 ± 0.07	18.57 ± 0.06	18.26 ± 0.21
366390.74 ± 1105.79	21.87 ± 0.07	21.17 ± 0.04	20.62 ± 0.03	20.15 ± 0.03	19.43 ± 0.06	18.89 ± 0.06	18.46 ± 0.15
448791.55 ± 1201.33	21.90 ± 0.08	21.27 ± 0.04	20.79 ± 0.04	20.33 ± 0.03	19.66 ± 0.07	18.97 ± 0.07	18.55 ± 0.18
537481.41 ± 1132.16	22.02 ± 0.09	21.52 ± 0.05	21.00 ± 0.04	20.55 ± 0.03	19.87 ± 0.07	19.20 ± 0.07	18.83 ± 0.17
794992.63 ± 1200.69	22.14 ± 0.04	21.51 ± 0.03	21.05 ± 0.04	20.71 ± 0.05	20.31 ± 0.13	19.79 ± 0.14	19.59 ± 0.41
1226716.84 ± 1050.15	22.17 ± 0.04	21.59 ± 0.04	21.26 ± 0.04	20.97 ± 0.04	20.34 ± 0.12	19.95 ± 0.11	19.40 ± 0.34

Extended Data Table 2: **GROND photometry.** $T_{\rm GROND}$ in seconds after the BAT trigger. The AB magnitudes are not corrected for the Galactic foreground reddening.

UTC	Instrument	Filter	Exposure (s)	Magnitude
2019-01-14.975	LT/IO:O	g	45	19.08±0.06
2019-01-14.976	LT/IO:O	r	45	18.22±0.02
2019-01-14.977	LT/IO:O	i	45	17.49±0.02
2019-01-14.978	LT/IO:O	z	45	17.12±0.02
2019-01-14.979	LT/IO:O	B	45	19.55±0.15
2019-01-14.980	LT/IO:O	V	45	18.81±0.08
2019-01-15.814	LT/IO:O	r	60	19.61±0.05
2019-01-15.818	LT/IO:O	z	60	18.70±0.06
2019-01-15.820	LT/IO:O	i	60	19.04±0.04
2019-01-15.823	LT/IO:O	g	60	20.96±0.17

Extended Data Table 3: **Liverpool Telescope observations.** Magnitudes are SDSS AB-"like" for ugriz, Vega-"like" for BV and are not corrected for Galactic extinction.

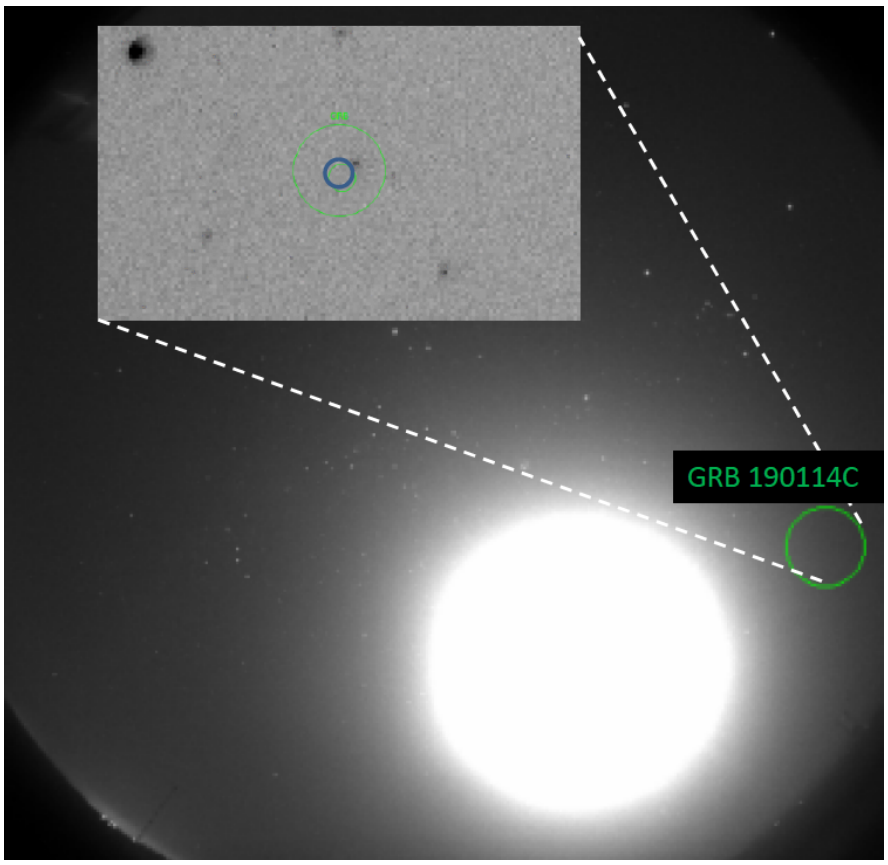

Extended Data Figure 4: **The CASANDRA-2 at the BOOTES-2 station all-sky image.** The image (30s exposure, unfiltered) was taken on Jan 14, 20:57:18 U.T. At the GRB190114C location (circle) no prompt optical emission is detected simultaneously to the gamma-ray photons (which started to arrive at 20:57:03 U.T.) See main text.

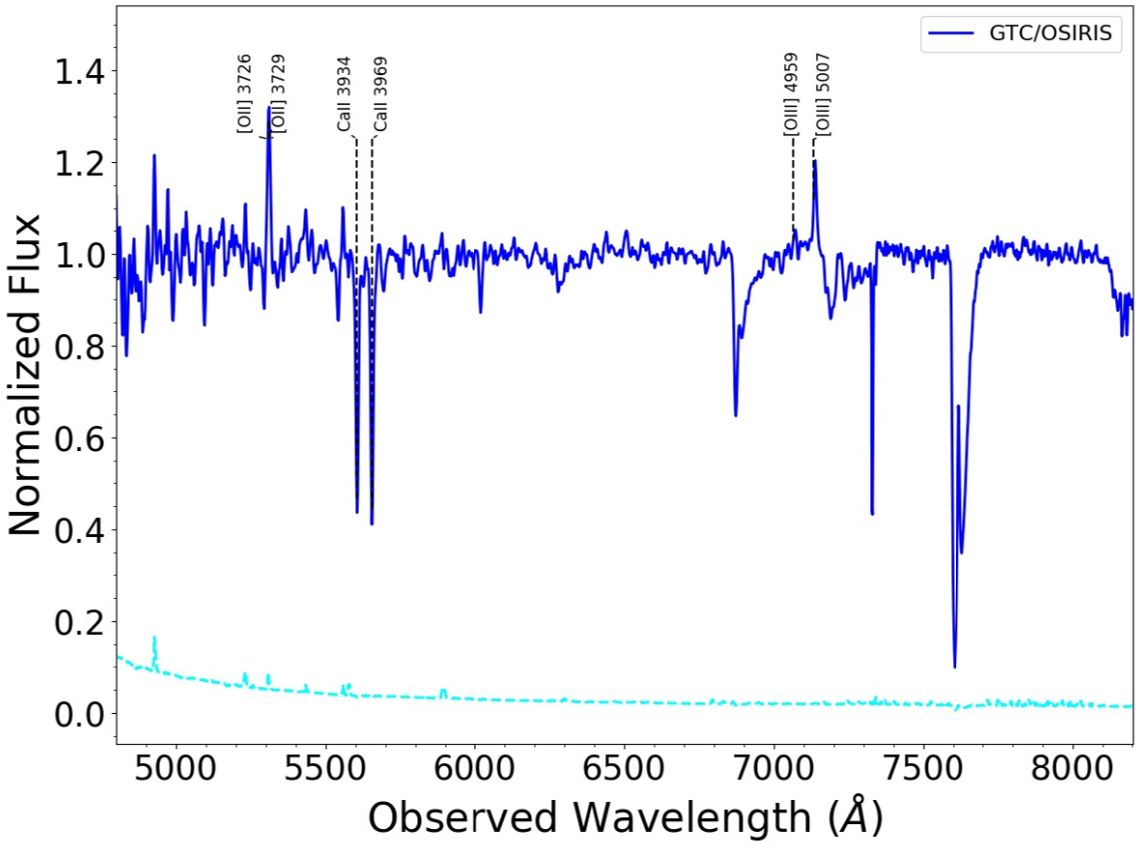

Extended Data Figure 5: **The GTC (+OSIRIS) spectrum.** The normalised spectrum of the GRB 190114C optical afterglow on Jan 14, 23:32:03 UT, taken with the R1000B and R2500I grisms. The emission lines of the underlying host galaxy are noticeable, besides the Ca II absorption lines in the afterglow spectrum (all of them are labelled). The cyan dotted line represents the noise. See main text.

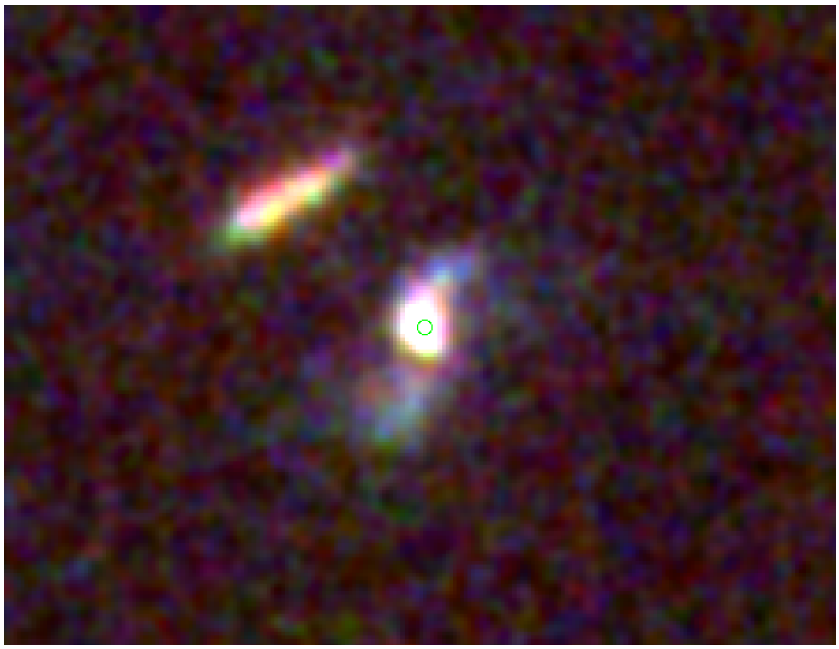

Extended Data Figure 6: **Three-colour image of the host of GRB 190114C with the HST.** The host galaxy is a spiral galaxy, and the green circle indicates the location of the transient close to its host nucleus. The image is $8''$ across, north is up and east to the left.

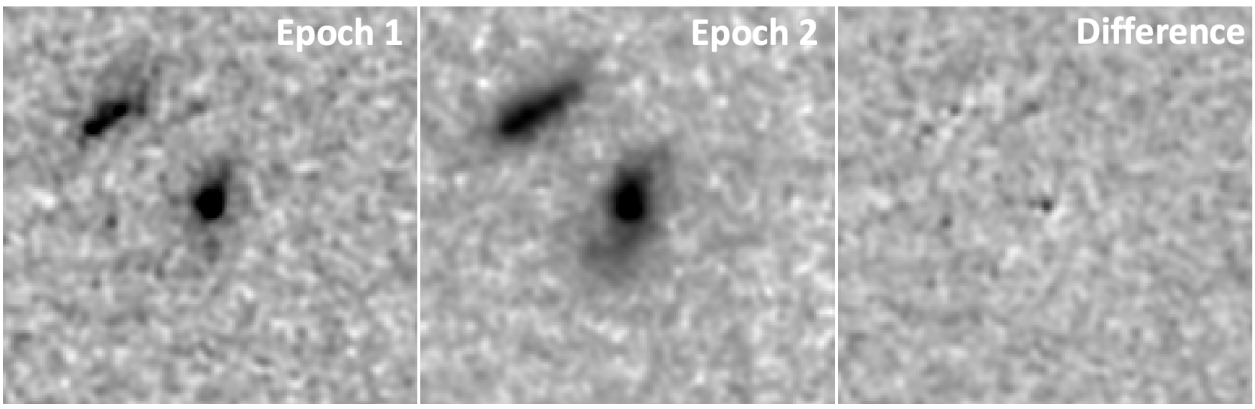

Extended Data Figure 7: **F850LP imaging of GRB 190114C taken with the HST.** Two epochs are shown (images are $4''$ across), as well as the result of the difference image. A faint transient is visible close to the nucleus of the galaxy, and we identify this as the late time afterglow of the burst.

NTT The ESO New Technology Telescope (NTT) observed the optical counterpart of GRB 190114C under the extended Public ESO Spectroscopic Survey for Transient Objects (ePESSTO) using the NTT/EFOSC2 instrument in imaging mode [62]. Observations started at 04:36:53 UT on 2019 January 16 with the g, r, i, z Gunn filters. Image reduction was carried out by following the standard procedures[63].

OASDG The 0.5 m remote telescope of the Osservatorio Astronomico "S. Di Giacomo" (OASDG), located in Agerola (Italy) started observations in the optical Rc-band 0.54 hours after the burst. The afterglow of GRB 190114C was clearly detected in all the images.

NOT The Nordic Optical Telescope (NOT) observed the optical afterglow of GRB 190114C with the Alhambra Faint Object Spectrograph and Camera (AlFOSC) instrument. Imaging was obtained

in the $griz$ filters with 300 s exposures, starting at Jan 14 21:20:56 UT, 24 minutes after the BAT trigger. The normalised spectrum (Extended Data Fig. 8) reveals strong host interstellar absorption lines due to Ca H & K and Na I D, which provided a redshift of $z = 0.425$.

REM The Rapid Eye Mount telescope (REM) performed optical and NIR observations with the REM 60 cm robotic telescope equipped with the ROS2 optical imager and the REMIR NIR camera[64]. Observations were performed starting about 3.8 hours after the burst in the r, and J bands and lasted about one hour.

***Swift*/UVOT** The *Swift* UltraViolet and Optical Telescope (UVOT[65]) began observations at T_0+54 seconds in the UVOT v band. The first observation after settling started 74 s after the trigger for 150 s in the UVOT $white$ band[66]. A 50 s exposure with the UV grism was taken thereafter, followed by multiple exposures rotating through all seven broad and intermediate-band filters until switching to only UVOT's clear white filter on 2019-01-20. Standard photometric calibration and methods were used for deriving the aperture photometry[67,68]. The grism zeroth order the data were reduced manually[69] to derive the b-magnitude and error.

VLT The STARGATE collaboration used the Very Large Telescope (VLT) and observed GRB 190114C using the X-shooter spectrograph. Detailed analysis will be presented in forthcoming papers. A portion of the second spectrum is shown in Extended Data Fig. 9, illustrating the strong emission lines characteristic of a strongly star-forming galaxy, whose light is largely dominating over the afterglow at this epoch.

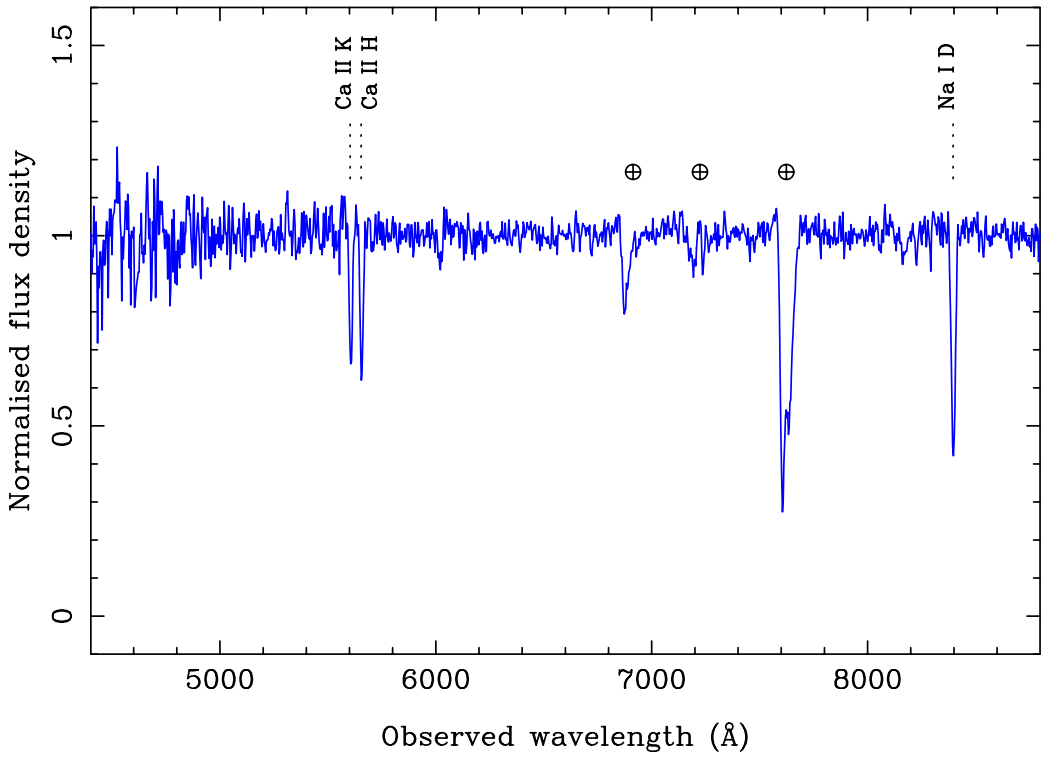

Extended Data Figure 8: **The NOT/AlFOSC spectrum.** The NOT/AlFOSC spectrum obtained at a mid-time 1 hr post-burst. The continuum is afterglow dominated at this time, and shows strong absorption features of Ca II and Na I (in addition to telluric absorption).

UTC	t-t_0 (d)	Filter	Exposure (s)	Magnitude (AB)
2019-01-14.89127	0.0183	g	1×300	17.72±0.03
2019-01-14.89512	0.0222	r	1×300	16.93±0.02
2019-01-14.89899	0.0260	i	1×300	16.42 ±0.04
2019-01-14.90286	0.0299	z	1×300	16.17 ±0.04
2019-01-23.8896	9.0167	i	6×300	21.02±0.05

Extended Data Table 4: **Nordic Optical Telescope/AlFOSC observations.** Magnitudes are in the SDSS AB system and are not corrected for Galactic extinction.

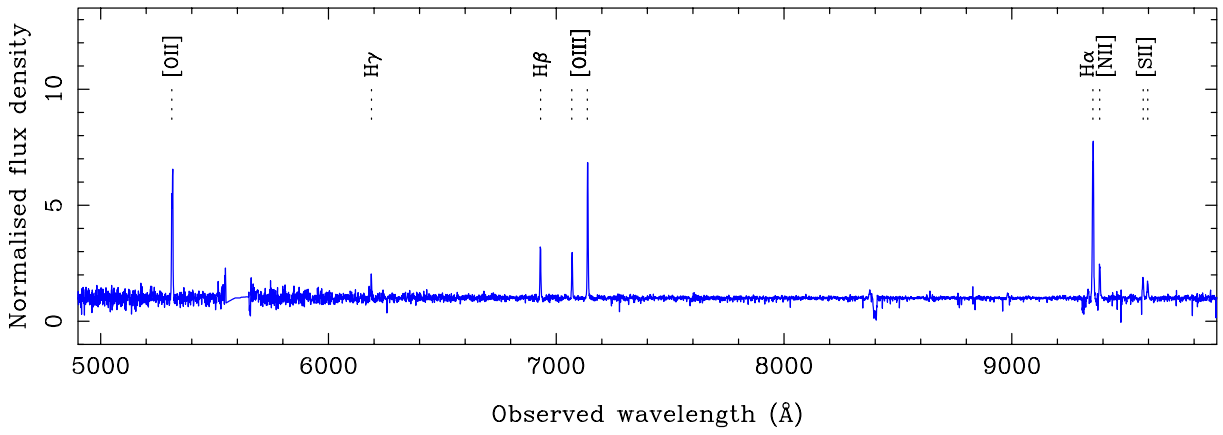

Extended Data Figure 9: **The VLT/X-shooter spectrum.** The visible light region of the VLT/X-shooter spectrum obtained approximately 3.2 d post-burst, showing strong emission lines from the star-forming host galaxy.

Magnitudes of the underlying galaxies The *HST* images show a spiral or tidally disrupted galaxy whose bulge is coincident with the coordinates of GRB 190114C. A second galaxy is detected at an angular distance of $1.3''$, towards the North East. The SED analysis was performed with LePhare [70,71] using an iterative method that combined both the resolved photometry of the two galaxies found in the *HST* and *VLT*/HAWK-I data and the blended photometry from *GALEX* and WISE, where the spatial resolution was much lower. Further details will be given in a paper in preparation (de Ugate Postigo et al.). The estimated photometry, for each object and their combination, is given in Extended Data Table 5.

Optical Extinction The optical extinction toward the line of sight of a GRB is derived assuming a a power law as intrinsic spectral shape[72]. Once the Galactic extinction ($E_{\rm B-V} = 0.01$[73]) is taken into account and the fairly bright host galaxy contribution is properly subtracted, a good fit to the data is obtained with the LMC recipe and $A_V = 1.83 \pm 0.15$. The spectral index β ($F_\nu \propto \nu^{\beta_{\rm o}}$) evolves from hard to soft across the temporal break in the optical light-curve at about 0.5 days, moving from $\beta_{\rm o,1} - 0.10 \pm 0.12$ to $\beta_{\rm o,2} - 0.48 \pm 0.15$.

Radio and Sub-mm afterglow observations

The light curves from the different instruments is shown in Extended Data Fig. 10.

ALMA The Atacama Large Millimetre/Submillimetre Array (ALMA) observations are reported in Band 3 (central observed frequency of 97.500 GHz) and Band 6 (235.0487 GHz), between 2019 January 15 and 2019 January 19. Data were calibrated within CASA (Common Astronomy Software Applications, version 5.4.0[74]) using the pipeline calibration. Photometric measurements were

Filter	Host	Companion	Combined
Sloan u	23.54	25.74	23.40
Sloan g	22.51	23.81	22.21
Sloan r	22.13	22.81	21.66
Sloan i	21.70	22.27	21.19
Sloan z	21.51	21.74	20.87
2MASS J	20.98	21.08	20.28
2MASS H	20.68	20.82	20.00
2MASS Ks	20.45	20.61	19.77

Extended Data Table 5: **Observations of the host galaxy.** For each filter, the estimated magnitudes are given for the host galaxy of GRB 190114C, the companion and the combination of the two objects.

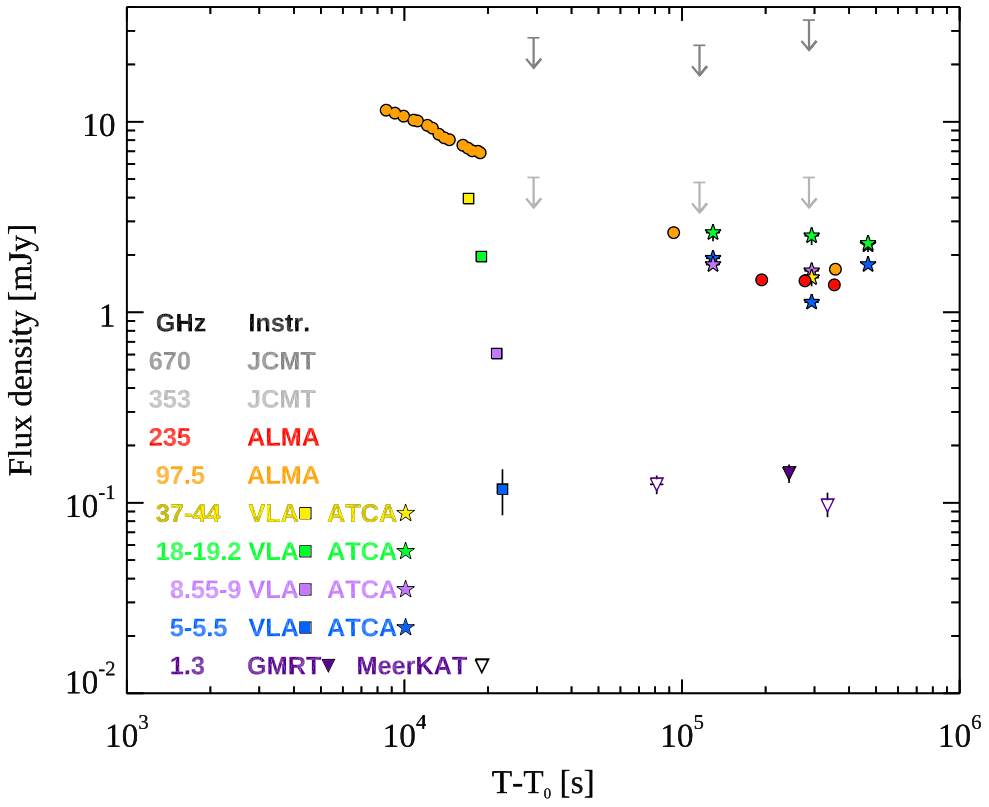

Extended Data Figure 10: **Radio and sub-mm observations GRB 190114C:** energy flux at different frequencies, from 1.3 GHz to 670 GHz, as a function of the time since the initial burst T_0.

also performed within CASA. ALMA early observations at 97.5 GHz are taken from [16].

ATCA The Australia Telescope Compact Array (ATCA)oObservations were made with the ATCA 4 cm receivers (band centres 5.5 and 9 GHz), 15 mm receivers (band centres 17 and 19 GHz), and 7 mm receivers (band centres 43 and 45 GHz). ATCA data were obtained using the CABB continuum mode [75] and reduced with the software packages MIRIAD [76] and CASA [74] using standard techniques. The quoted errors are 1σ, which include the RMS and Gaussian 1σ errors.

GMRT The upgraded Giant Metre-wave Radio Telescope [77] (UGMRT) observed on 17th January 2019 13.44 UT (2.8 days after the burst) in band 5 (1000-1450 MHz) with 2048 channels spread over 400 MHz. GMRT detected a weak source with a flux density of 73 ± 17 μJy at the GRB position [78]. The flux should be considered as an upper limit, as the contribution from the host[79] has not been subtracted.

MeerKAT The new MeerKAT radio observatory [80,81] observed on 15 and 18 January 2019, with DDT requested by the ThunderKAT Large Survey Project [82]. Both epochs used 63 antennas and were done at L-band spanning 856 MHz and centered at 1284 MHz. MeerKAT flux estimation was done by finding and fitting the source with the software PyBDSF v.1.8.15 [83].Adding the RMS noise in quadrature to the flux uncertainty leads to final flux measurements of 125 ± 14 μJy/beam on 15 January and 97 ± 16 μJy/beam on 18 January. The contribution from the host galaxy[79] has not been subtracted. Therefore, these measurements provide a maximum flux of the GRB.

JCMT SCUBA-2 Sub-millimeter Sub-millimeter observations were performed simultaneously at 850 μm and 450 μm on three nights using the SCUBA-2 continuum camera[84]. GRB 190114C

Start Date and Time	End Date and Time	Frequency GHz	Flux mJy
1/16/2019 6:47:00	1/16/2019 10:53:00	5.5	1.92±0.06
		9	1.78±0.06
		18	2.62±0.26
1/18/2019 1:45:00	1/18/2019 11:18:00	5.5	1.13±0.04
		9	1.65±0.05
		18	2.52±0.27
		44	1.52±0.15
1/20/2019 3:38	1/20/2019 10:25:00	5.5	1.78±0.06
		9	2.26±0.07
		18	2.30±0.23

Extended Data Table 6: **Observations by ATCA**. Start and end date and times (UTC) of the observations, frequency, and flux (1σ error).

UT Date	Time since trigger (days)	Time on source (hours)	Typical 225 GHz CSO Opacity[a]	Typical elevation (degrees)	850 μm RMS density (mJy/beam)	450 μm RMS density (mJy/beam)
2019-01-15	0.338	1.03	0.026	39	1.7	9.2
2019-01-16	1.338	1.03	0.024	39	1.6	8.4
2019-01-18	3.318	0.95	0.031	37	1.7	11.4

Extended Data Table 7: **JCMT SCUBA-2 sub-millimeter observations of GRB 190114C.**

[a]The CSO 225 GHz tau measures the zenith atmospheric attenuation.

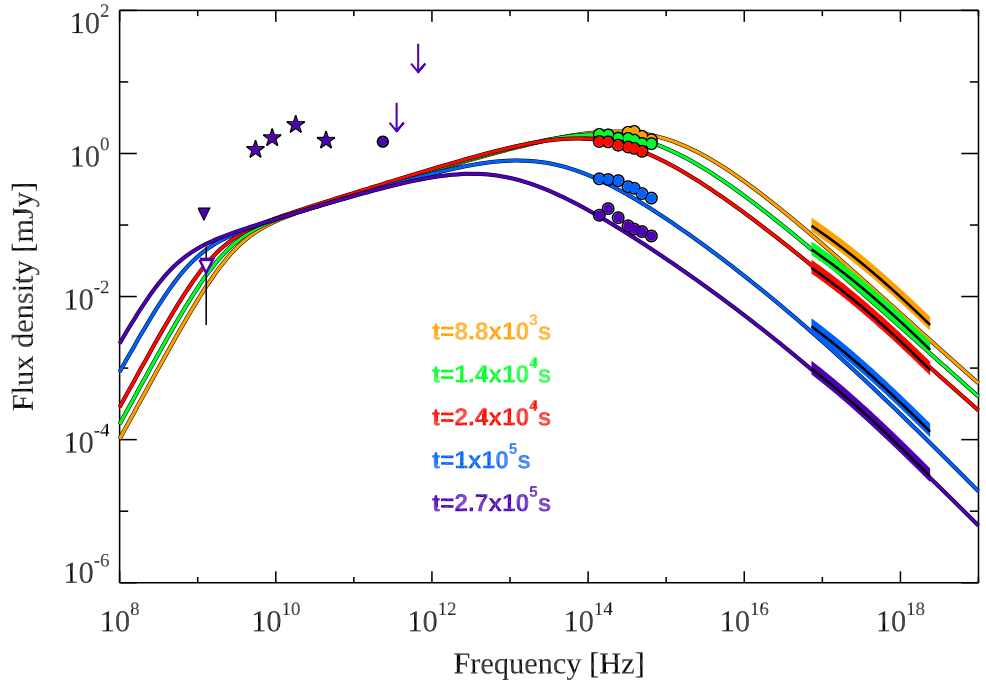

Extended Data Figure 11: **Radio to X-rays SED at different epochs**. The synchrotron frequency $\nu_{\rm m}$ crosses the optical band, moving from higher to lower frequencies. The break between 10^8 and 10^{10} Hz is caused by the self-absorption synchrotron frequency $\nu_{\rm sa}$. Optical (X-ray) data have been corrected for extinction (absorption).

was not detected on any of the individual nights. Combining all the SCUBA-2 continuum camera[84] observations, the RMS background noise is 0.95 mJy/beam at 850 μm and 5.4 mJy/beam at 450 μm at 1.67 days after the burst trigger.

Prompt emission model for the early time MAGIC emission In the standard picture the prompt sub-MeV spectrum is explained as a synchrotron radiation from relativistic accelerated electrons in the energy dissipation region. The associated inverse Compton component is sensitive to the details

of the dynamics: e.g. in the internal shock model if the peak energy is initially very high and the IC component is suppressed due to Klein-Nishina (KN) effects, the peak of the IC component may be delayed and become bright only at late times when scatterings occur in Thomson regime. Simulations showed that magnetic fields required to produce the GeV/TeV component are rather low[85], $\epsilon_B \sim 10^{-3}$. In this framework the contribution of the IC component to the observed flux at early times (62-90 s, see Extended Data Table 1) does not exceed $\sim 20\%$. Alternatively, if the prompt emission originates in reprocessed photospheric emission, the early TeV flux may arise from IC scatterings of thermal photons by freshly heated electrons below the photosphere at low optical depths. Another possibility for the generation of TeV photons might be the IC scattering of prompt MeV photons by electrons in the external forward shock region where electrons are heated to an average Lorentz factor of order 10^4 at early times.

Afterglow model Synchrotron and SSC radiation from electrons accelerated at the forward shock has been modelled within the external shock scenario [7,8,20,25,86]. The results of the modeling are overlaid to the data in Fig. 3, and Extended Data Figs. 11 and 12.

We consider two types of power law radial profiles $n(R) = n_0\, R^{-s}$ for the external environment: $s = 0$ (homogeneous medium) and $s = 2$ (wind-like medium, typical of an environment shaped by the stellar wind of the progenitor). In the last case, we define $n_0 = 3 \times 10^{35}\, A_\star\, \mathrm{cm}^{-1}$. We assume that electrons swept up by the shock are efficiently accelerated into a PL distribution described by spectral index p: $dN/d\gamma_\mathrm{e} \propto \gamma_\mathrm{e}^{-p}$, where γ_e is the electron Lorentz factor. We call ν_m the characteristic synchrotron frequency of electrons with Lorentz factor γ_m, ν_c the cooling frequency, and ν_sa the synchrotron self-absorption frequency.

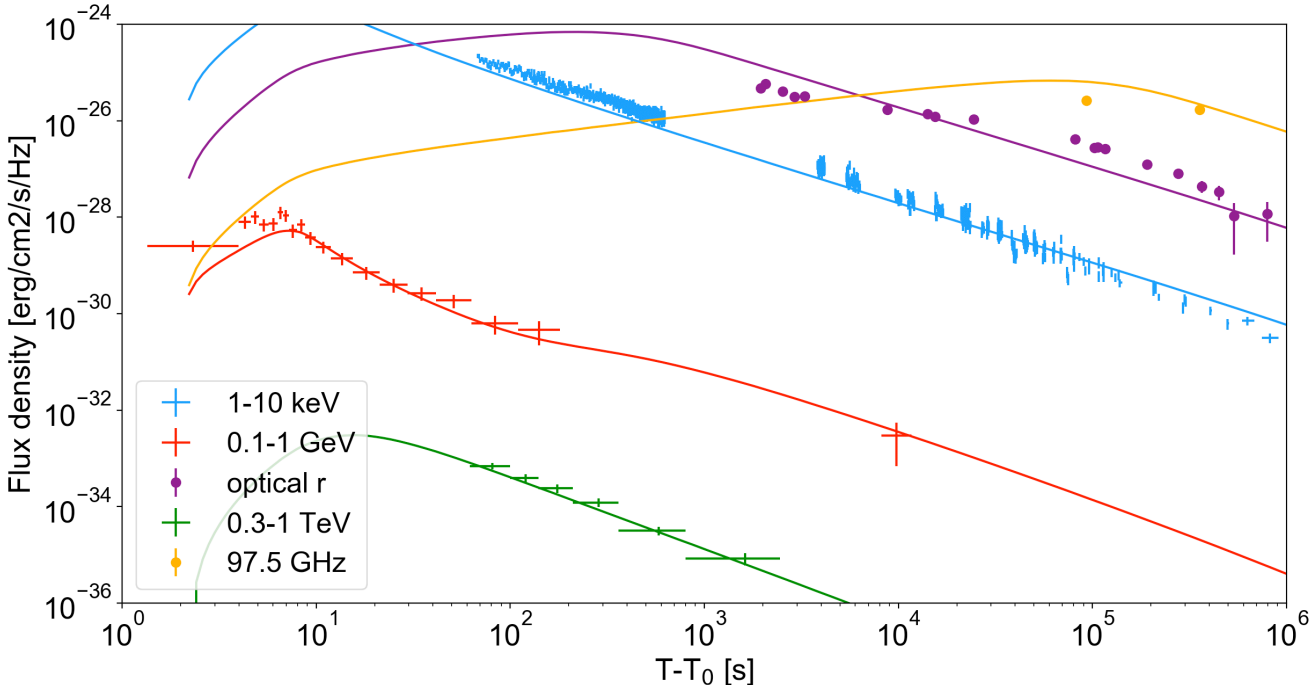

Extended Data Figure 12: **PRELIMINARY - Modeling of the broadband light curves.** Modeling of forward shock emission (solid curves) is compared to observations, at different frequencies (see legend). **This is for $s = 0$. The new modeling for $s = 2$ will be added.**

The early time optical emission (up to $\sim$ 1000 s) and radio emission (up to $\sim 10^5$ s) are most likely dominated by reverse shock radiation [16]. Detailed modeling of this component is not discussed in this work, where we focus on forward shock radiation.

The XRT flux (Fig. 1, blue data points) decays as $F_{\rm X} \propto t^{\alpha_{\rm X}}$ with $\alpha_{\rm X} = -1.36 \pm 0.02$. If $\nu_{\rm X} > max(\nu_{\rm m}, \nu_{\rm c})$, the X-ray light curve is predicted to decay as $t^{(2-3p)/4}$, that implies $p \sim 2.5$. Another possibility is to assume $\nu_{\rm m} < \nu_{\rm X} < \nu_{\rm c}$ for the whole observing time, which implies a slow cooling regime and $p = 2.1 - 2.2$ to explain the temporal decay. A broken power law fit provides a better fit (5.3×10^{-5} probability of chance improvement), with a break occurring around 4×10^4 s

and decay indices $\alpha_{\rm X,1} \sim -1.32 \pm 0.03$ and $\alpha_{\rm X,2} \sim -1.55 \pm 0.04$. This behaviour can be explained if the electrons are in a slow cooling regime at the time of the break, and assuming $p = 2.7$ for $s = 0$, and $p = 2.4 - 2.5$ for $s = 2$. In both cases, the temporal break can be explained by the frequency $\nu_{\rm c}$ crossing the XRT band.

From $\sim 2 \times 10^3$ s the optical light curve starts displaying a shallow decay in time (with temporal index poorly constrained, between -0.5 and -0.25), followed by a steepening around 8×10^4 s, when the temporal decay becomes similar to the decay in X-ray band, suggesting that after this time the X-ray and optical band lie in the same part of the synchrotron spectrum. If the break is interpreted as the synchrotron characteristic frequency $\nu_{\rm m}$ crossing the optical band, after the break the observed temporal decay requires a very steep value of $p \sim 3$ for $s = 0$ and a value between $p = 2.4$ and $p = 2.5$ for $s = 2$. This interpretation implies (independently of the density profile of the external medium and on the cooling regime of the electrons) that $\nu_{\rm m}$ is in the X-ray band at 10^2 s:

$$\nu_{\rm m}(t = 8 \times 10^4\,) = 3 \times 10^{18}\,{\rm Hz} \left(\frac{t}{100\,{\rm s}} \right)^{-1.5} = 10^{14}\,{\rm Hz}\,. \quad (1)$$

The SED at ~100 s is indeed characterised by a peak in between 5-30 keV (Fig. 3), that we interpret as the characteristic synchrotron frequency $\nu_{\rm m}$. **Observations at 1 GHz provide information on the location of the synchrotron self-absorption frequency, that is located at** $\nu_{\rm sa} \sim 1$ **GHz at** 10^5 **s (Extended Data Fig. 11)**.

Summarizing, **in a wind-like scenario** X-ray and optical emission and their evolution in time can be explained if $p = 2.4 - 2.5$, the emission is initially in fast cooling regime and transitions to a slow cooling regime around 3×10^3 s. The optical spectral index at late times is predicted to be

$(1-p)/2 \sim -0.72$, in agreement with observations. $\nu_{\rm m}$ crosses the optical band at $t \sim 8 \times 10^4$ s, explaining the steepening of the optical light curve and the flattening of the optical spectrum. The X-ray band initially lies above (or close to) $\nu_{\rm m}$, and the break frequency $\nu_{\rm c}$ starts crossing the X-ray band around $2-4 \times 10^4$ s, producing the steepening in the decay rate (the cooling frequency increases with time for $s = 2$). In this case, before the temporal break, the decay rate is related to the spectral index of the electron energy distribution by $\alpha_{\rm X,1} = (2-3p)/4 \sim -1.3$, for $p \sim 2.4-2.5$. Well after the break, this value of p predicts a decay rate $\alpha_{\rm X,1} = (1-3p)/4 = -1.55 - 1.62$. Overall, this interpretation is also consistent with the fact that the late time ($t > 10^5$ s) X-ray and optical light curves display similar temporal decays (Fig.1), as they lie in the same part of the synchrotron spectrum ($\nu_{\rm m} < \nu_{\rm opt} < \nu_{\rm X} < \nu_{\rm c}$).

Alternatively, **assuming a homogeneous density medium**, observations can be modeled if $\nu_{\rm c} > \nu_{\rm m}$ at all times, implying that the emission is always produced in a slow cooling regime **to be completed with the details of the $s = 0$ modeling**.

We now add to the picture the information brought by the TeV detection. The modeling is built with reference to the MAGIC flux and spectral indices derived considering statistical errors only (see Extended Data Table 1 and green data points in Extended Data Fig. 2). **The light curve decays in time as $t^{-1.51}$ and the photon index is consistent within $\sim 1\sigma$ with $\Gamma_{\rm ph,TeV} \sim -2.5$ for the entire duration of the emission, although there is evidence for an evolution from harder (~ -2) to softer (~ -2.8) values.** In the first broadband SED (Fig. 3, upper panel), LAT observations provide strong evidence for the presence of two separated spectral peaks.

Assuming Thomson scattering, the SSC peak is given by:

$$\nu_{\rm peak}^{\rm SSC} \simeq 2\,\gamma_{\rm e}^2 \nu_{\rm peak}^{\rm syn} \tag{2}$$

while in KN regime, the SSC peak should be located at:

$$h\nu_{\rm peak}^{\rm SSC} \simeq 2\,\gamma_{\rm e}\,\Gamma\,m_{\rm e}\,c^2/(1+z) \tag{3}$$

where $\gamma_{\rm e} = \min(\gamma_{\rm c}, \gamma_{\rm m})$. The synchrotron spectral peak is located at $E_{\rm peak}^{\rm syn} \sim 10\,{\rm keV}$, while the peak of the SSC component must be below $E_{\rm peak}^{\rm ssc} \lesssim 100\,{\rm GeV}$ to explain the MAGIC photon index. Both the KN and Thomson scattering regimes imply $\gamma_{\rm e} \lesssim 10^3$. This small value faces two problems: i) if the bulk Lorentz factor Γ is larger than 150 (that is a necessary condition to avoid strong γ-γ opacity, see below), a small $\gamma_{\rm m}$ translates into a small efficiency of the electron acceleration, with $\epsilon_{\rm e} < 0.05$, ii) the synchrotron peak energy can be located at $E_{\rm peak}^{\rm syn} \sim 10\,{\rm keV}$ only for $B\,\Gamma \gtrsim 10^5\,{\rm G}$.

These calculations show that γ-γ opacity likely plays an role in shaping the observed peak energy of the SSC spectrum[87,88].

For a gamma-ray photon with energy E_γ, the $\tau_{\gamma\gamma}$ opacity is:

$$\tau_{\gamma\gamma}(E_\gamma) = \sigma_{\gamma\gamma}\,(R/\Gamma)\,n_{\rm t}(E_\gamma)\,, \tag{4}$$

where $n_{\rm t} = L_{\rm t}/(4\,\pi\,R^2\,c\,\Gamma\,E_{\rm t})$ is the density of target photons in the comoving frame, $L_{\rm t}$ is the luminosity and $E_{\rm t} = (m_{\rm e}\,c^2)^2\,\Gamma^2/E_\gamma/(1+z)^2$ is the energy of target photons in the observer frame. Target photons for photons with energy $E_\gamma = 0.2 - 1\,{\rm TeV}$ and for $\Gamma \sim 120 - 150$ have energies in the range $4 - 30\,{\rm keV}$. **When $\gamma - \gamma$ absorption is relevant, the emission from the pairs can give a non-negligible contribution to the radiative output.**

To properly model all the physical processes that are shaping the broad band radiation, we build a numerical code that solves the evolution of the electron distributions and derive the radiative output taking into account the following processes: synchrotron and SSC losses, adiabatic losses, $\gamma - \gamma$ absorption, emission from the pairs, and synchrotron self-absorption[89–92]. We find that for the parameters assumed in the proposed modeling (see below), the contribution from pairs to the emission is negligible.

The MAGIC photon index (Extended Data Table 1) and its evolution with time constrains in any case the SSC peak energy to be not much higher than 1 TeV: in general the internal opacity decreases with time and KN effects become less relevant. A possible softening of the spectrum with time, as the one suggested by the observations, requires that the spectral peak decreases with time and crosses the MAGIC energy range. As the SSC spectrum is very broad around the peak, KN and/or opacity still need to play a role also at late times ($\sim 2000\,\mathrm{s}$) in order to explain soft photon indices $\Gamma_{\rm TeV} < -2$ (Extended Data Table 1). In the slow cooling regime, the SSC peak evolves to higher frequencies for a wind-like medium and decreases very slowly ($\nu_{\rm peak}^{\rm SSC} \propto t^{-1/4}$) for a constant-density medium (both in KN and Thomson regimes). In fast cooling regime the evolution is faster ($\nu_{\rm peak}^{\rm SSC} \propto t^{-1/2} - t^{-9/4}$ depending on medium and regime).

We model the broadband observations **considering both** $s = 0$ **and** $s = 2$. The results are shown in Extended Data Fig. 12. **We find that the fast temporal decay rate of the TeV light curve can be more easily explained in a homogeneous medium.**

The results of the broad band modeling is shown in Fig.3, and Extended Data Figs. 11 and

12 where model curves are overlaid to observations. The model curves shown in these figures have been derived using the following parameters: $\epsilon_{\rm e}$ =??, $\epsilon_{\rm B}$ =??, $\xi_{\rm e}$ =??, p =??, $n_{0}\star$ =??, and $E_{\rm k}$ =??. Using the constraints on the afterglow onset time ($t^{\rm aft}_{\rm peak} \sim 5 - 10\,{\rm s}$ from the smooth component detected during the prompt emission) the initial bulk Lorentz factor is constrained to assume values $\Gamma_0 \sim 300$ and $\Gamma_0 \sim 700$ for $s = 2$ and $s = 0$, respectively.

1. Mészáros, P. Theories of Gamma-Ray Bursts. ARA&A **40**, 137–169 (2002). astro-ph/0111170.

2. Piran, T. The physics of gamma-ray bursts. *Reviews of Modern Physics* **76**, 1143–1210 (2004). astro-ph/0405503.

3. Gehrels, N., Ramirez-Ruiz, E. & Fox, D. B. Gamma-Ray Bursts in the Swift Era. ARA&A **47**, 567–617 (2009). 0909.1531.

4. Gehrels, N. & Mészáros, P. Gamma-Ray Bursts. *Science* **337**, 932 (2012). 1208.6522.

5. Kumar, P. & Zhang, B. The physics of gamma-ray bursts & relativistic jets. Phys. Rep. **561**, 1–109 (2015). 1410.0679.

6. van Paradijs, J., Kouveliotou, C. & Wijers, R. A. M. J. Gamma-Ray Burst Afterglows. ARA&A **38**, 379–425 (2000).

7. Sari, R., Piran, T. & Narayan, R. Spectra and Light Curves of Gamma-Ray Burst Afterglows. ApJ **497**, L17–L20 (1998). astro-ph/9712005.

8. Granot, J. & Sari, R. The Shape of Spectral Breaks in Gamma-Ray Burst Afterglows. ApJ **568**, 820–829 (2002). astro-ph/0108027.

9. Meszaros, P. & Rees, M. J. Delayed GEV Emission from Cosmological Gamma-Ray Bursts - Impact of a Relativistic Wind on External Matter. MNRAS **269**, L41 (1994). astro-ph/9404056.

10. MAGIC-Collaboration. Teraelectronvolt emission from a gamma-ray burst. *Nature* (2019).

11. The Milagro Collaboration: R. Atkins *et al.* Evidence for TeV Emission from GRB 970417a. *arXiv e-prints* astro–ph/0001111 (2000). astro-ph/0001111.

12. Nava, L. High-energy emission from gamma-ray bursts. *International Journal of Modern Physics D* **27**, 1842003 (2018). 1804.01524.

13. Mirzoyan, R. First time detection of a GRB at sub-TeV energies; MAGIC detects the GRB 190114C. *The Astronomer's Telegram* **12390** (2019).

14. Fermi & collaboration, S. GRB190114C. *journal* (2019).

15. Ravasio, M. E. *et al.* GRB 190114C: from prompt to afterglow? *arXiv e-prints* (2019). 1902.01861.

16. Laskar, T. *et al.* ALMA Detection of a Linearly Polarized Reverse Shock in GRB 190114C. *arXiv e-prints* (2019). 1904.07261.

17. Vietri, M. GeV Photons from Ultrahigh Energy Cosmic Rays Accelerated in Gamma Ray Bursts. *Physical Review Letters* **78**, 4328–4331 (1997). astro-ph/9705061.

497 18. Zhang, B. & Mészáros, P. High-Energy Spectral Components in Gamma-Ray Burst After-
498 glows. ApJ **559**, 110–122 (2001). astro-ph/0103229.

499 19. Razzaque, S. A Leptonic-Hadronic Model for the Afterglow of Gamma-ray Burst 090510.
500 ApJ **724**, L109–L112 (2010). 1004.3330.

501 20. Sari, R. & Esin, A. A. On the Synchrotron Self-Compton Emission from Relativistic
502 Shocks and Its Implications for Gamma-Ray Burst Afterglows. ApJ **548**, 787–799 (2001).
503 astro-ph/0005253.

504 21. Mészáros, P., Razzaque, S. & Zhang, B. GeV-TeV emission from γ-ray bursts. New A Rev.
505 **48**, 445–451 (2004).

506 22. Gupta, N. & Zhang, B. Prompt emission of high-energy photons from gamma ray bursts.
507 MNRAS **380**, 78–92 (2007). 0704.1329.

508 23. Fan, Y.-Z. & Piran, T. High-energy γ-ray emission from gamma-ray bursts — before GLAST.
509 *Frontiers of Physics in China* **3**, 306–330 (2008). 0805.2221.

510 24. Galli, A. & Piro, L. Prospects for detection of very high-energy emission from GRB in the
511 context of the external shock model. A&A **489**, 1073–1077 (2008). 0805.2884.

512 25. Nakar, E., Ando, S. & Sari, R. Klein-Nishina Effects on Optically Thin Synchrotron and
513 Synchrotron Self-Compton Spectrum. ApJ **703**, 675–691 (2009). 0903.2557.

514 26. Xue, R. R. *et al.* Very High Energy γ-Ray Afterglow Emission of Nearby Gamma-Ray Bursts.
515 ApJ **703**, 60–67 (2009). 0907.4014.

516 27. Piran, T. & Nakar, E. On the External Shock Synchrotron Model for Gamma-ray Bursts' GeV
517 Emission. ApJ **718**, L63–L67 (2010). 1003.5919.

518 28. Ackermann, M. *et al.* Fermi-LAT Observations of the Gamma-Ray Burst GRB 130427A.
519 *Science* **343**, 42–47 (2014). 1311.5623.

520 29. Liu, R.-Y., Wang, X.-Y. & Wu, X.-F. Interpretation of the Unprecedentedly Long-lived High-
521 energy Emission of GRB 130427A. ApJ **773**, L20 (2013). 1306.5207.

522 30. Tam, P.-H. T., Tang, Q.-W., Hou, S.-J., Liu, R.-Y. & Wang, X.-Y. Discovery of an Extra Hard
523 Spectral Component in the High-energy Afterglow Emission of GRB 130427A. ApJ **771**, L13
524 (2013). 1305.3217.

525 31. Hamburg, R. GRB 190114C: Fermi GBM detection. *GRB Coordinates Network, Circular*
526 *Service, No. 23707, #1 (2019/January-0)* **23707** (2019).

527 32. Kocevski, D. *et al.* GRB 190114C: Fermi-LAT detection. *GRB Coordinates Network* **23709**,
528 1 (2019).

529 33. Gropp, J. D. GRB 190114C: Swift detection of a very bright burst with a bright optical
530 counterpart. *GRB Coordinates Network, Circular Service, No. 23688, #1 (2019/January-0)*
531 **23688** (2019).

532 34. Ursi, A. *et al.* GRB 190114C: AGILE/MCAL detection. *GRB Coordinates Network* **23712**, 1
533 (2019).

534 35. Frederiks, D. *et al.* Konus-Wind observation of GRB 190114C. *GRB Coordinates Network*
535 **23737**, 1 (2019).

536 36. Minaev, P. & Pozanenko, A. GRB 190114C: SPI-ACS/INTEGRAL extended emission detec-
537 tion. *GRB Coordinates Network* **23714**, 1 (2019).

538 37. Xiao, S. *et al.* GRB 190114C:Insight-HXMT/HE detection. *GRB Coordinates Network* **23716**,
539 1 (2019).

540 38. Tavani, M. *et al.* The AGILE Mission. *Astron. Astrophys.* **502**, 995–1013 (2009).

541 39. Goldstein, A. *et al.* The Fermi GBM Gamma-Ray Burst Spectral Catalog: The First Two
542 Years. ApJS **199**, 19 (2012). 1201.2981.

543 40. Meegan, C. *et al.* The Fermi Gamma-ray Burst Monitor. ApJ **702**, 791–804 (2009). 0908.
544 0450.

545 41. Barthelmy, S. D. *et al.* The Burst Alert Telescope (BAT) on the SWIFT Midex Mission.
546 Space Sci. Rev. **120**, 143–164 (2005). astro-ph/0507410.

547 42. Atwood, A. A., W. B.Abdo *et al.* The Large Area Telescope on the Fermi Gamma-Ray Space
548 Telescope Mission. ApJ **697**, 1071–1102 (2009). 0902.1089.

549 43. Kocevski, D. *et al.* GRB 190114C: Fermi-LAT detection. *GRB Coordinates Network* **23709**,
550 1 (2019).

551 44. Aleksić, J. *et al.* The major upgrade of the MAGIC telescopes, Part II: A performance study
552 using observations of the Crab Nebula. *Astroparticle Physics* **72**, 76–94 (2016). 1409.5594.

553 45. Ahnen, M. L. *et al.* Performance of the MAGIC telescopes under moonlight. *Astroparticle*
554 *Physics* **94**, 29–41 (2017). 1704.00906.

555 46. Domínguez, A. *et al.* Extragalactic background light inferred from AEGIS galaxy-SED-type
556 fractions. MNRAS **410**, 2556–2578 (2011). 1007.1459.

557 47. Franceschini, A., Rodighiero, G. & Vaccari, M. Extragalactic optical-infrared background ra-
558 diation, its time evolution and the cosmic photon-photon opacity. A&A **487**, 837–852 (2008).
559 0805.1841.

560 48. Finke, J. D., Razzaque, S. & Dermer, C. D. Modeling the Extragalactic Background Light
561 from Stars and Dust. ApJ **712**, 238–249 (2010). 0905.1115.

562 49. Gilmore, R. C., Somerville, R. S., Primack, J. R. & Domínguez, A. Semi-analytic modelling
563 of the extragalactic background light and consequences for extragalactic gamma-ray spectra.
564 MNRAS **422**, 3189–3207 (2012). 1104.0671.

565 50. UK *Swift* Science Data Centre. GRB 190114C *Swift*/XRT Light Curve. https://www.
566 swift.ac.uk/xrt_curves/00883832/.

567 51. Evans, P. A. *et al.* Methods and results of an automatic analysis of a complete sample of
568 Swift-XRT observations of GRBs. MNRAS **397**, 1177–1201 (2009). 0812.3662.

569 52. Greiner, J. *et al.* GROND—a 7-Channel Imager. *Publications of the Astronomical Society of*
570 *the Pacific* **120**, 405 (2008). 0801.4801.

571 53. Tody, D. IRAF in the Nineties. In Hanisch, R. J., Brissenden, R. J. V. & Barnes, J. (eds.)
572 *Astronomical Data Analysis Software and Systems II*, vol. 52 of *Astronomical Society of the*
573 *Pacific Conference Series*, 173 (1993).

574 54. Krühler, T. *et al.* The 2175 Å Dust Feature in a Gamma-Ray Burst Afterglow at Redshift 2.45.
575 ApJ **685**, 376–383 (2008). 0805.2824.

576 55. Bolmer, J. *et al.* Dust reddening and extinction curves toward gamma-ray bursts at $z > 4$.
577 A&A **609**, A62 (2018). 1709.06867.

578 56. Castro-Tirado, A. J. *et al.* A very sensitive all-sky CCD camera for continuous recording of
579 the night sky. In Proc. SPIE, vol. 7019 of *Society of Photo-Optical Instrumentation Engineers*
580 *(SPIE) Conference Series*, 70191V (2008).

581 57. Cepa, J. *et al.* OSIRIS tunable imager and spectrograph. In Iye, M. & Moorwood, A. F. (eds.)
582 *Optical and IR Telescope Instrumentation and Detectors*, vol. 4008 of Proc. SPIE, 623–631
583 (2000).

584 58. Castro-Tirado, A. GRB 190114C: refined redshift by the 10.4m GTC. *GRB Coordinates*
585 *Network, Circular Service, No. 23708, #1 (2019/January-0)* **23708** (2019).

586 59. de Ugarte Postigo, A. *et al.* The distribution of equivalent widths in long GRB afterglow
587 spectra. A&A **548**, A11 (2012). 1209.0891.

588 60. Steele, I. A. *et al.* The Liverpool Telescope: performance and first results. In Oschmann, J. M.,
589 Jr. (ed.) *Ground-based Telescopes*, vol. 5489 of Proc. SPIE, 679–692 (2004).

590 61. Chambers, K. C. *et al.* The Pan-STARRS1 Surveys. *arXiv e-prints* (2016). 1612.05560.

591 62. Tarenghi, M. & Wilson, R. N. The ESO NTT (New Technology Telescope): The first active
592 optics telescope. In Roddier, F. J. (ed.) *Active telescope systems*, vol. 1114 of *Society of Photo-*
593 *Optical Instrumentation Engineers (SPIE) Conference Series*, 302–313 (1989).

594 63. Smartt, S. J. *et al.* PESSTO: survey description and products from the first data release by the
595 Public ESO Spectroscopic Survey of Transient Objects. A&A **579**, A40 (2015). 1411.0299.

596 64. Covino, S. *et al.* REM: a fully robotic telescope for GRB observations. In Moorwood, A.
597 F. M. & Iye, M. (eds.) *Ground-based Instrumentation for Astronomy*, vol. 5492 of *Society of*
598 *Photo-Optical Instrumentation Engineers (SPIE) Conference Series*, 1613–1622 (2004).

599 65. Roming, P. W. A. *et al.* The Swift Ultra-Violet/Optical Telescope. Space Sci. Rev. **120**, 95–142
600 (2005). astro-ph/0507413.

601 66. Siegel, M. H. & Gropp, J. D. GRB 190114C: Swift/UVOT Detection. *GRB Coordinates*
602 *Network* **23725**, 1 (2019).

603 67. Poole, T. S. *et al.* Photometric calibration of the Swift ultraviolet/optical telescope. MNRAS
604 **383**, 627–645 (2008). 0708.2259.

605 68. Breeveld, A. A. *et al.* An Updated Ultraviolet Calibration for the Swift/UVOT. In *American*
606 *Institute of Physics Conference Series*, vol. 1358, 373–376 (2011). 1102.4717.

607 69. Kuin, N. P. M. *et al.* Calibration of the Swift-UVOT ultraviolet and visible grisms. MNRAS
608 **449**, 2514–2538 (2015).

609 70. Arnouts, S. *et al.* Measuring and modelling the redshift evolution of clustering: the Hubble
610 Deep Field North. MNRAS **310**, 540–556 (1999). astro-ph/9902290.

611 71. Ilbert, O. *et al.* Accurate photometric redshifts for the CFHT legacy survey calibrated using
612 the VIMOS VLT deep survey. A&A **457**, 841–856 (2006). astro-ph/0603217.

613 72. Covino, S. *et al.* Dust extinctions for an unbiased sample of gamma-ray burst afterglows.
614 MNRAS **432**, 1231–1244 (2013). 1303.4743.

615 73. Schlafly, E. F. & Finkbeiner, D. P. Measuring Reddening with Sloan Digital Sky Survey Stellar
616 Spectra and Recalibrating SFD. ApJ **737**, 103 (2011). 1012.4804.

617 74. McMullin, J. P., Waters, B., Schiebel, D., Young, W. & Golap, K. CASA Architecture and
618 Applications. In Shaw, R. A., Hill, F. & Bell, D. J. (eds.) *Astronomical Data Analysis Soft-*
619 *ware and Systems XVI*, vol. 376 of *Astronomical Society of the Pacific Conference Series*, 127
620 (2007).

621 75. Wilson, W. E. *et al.* The Australia Telescope Compact Array Broad-band Backend: description
622 and first results. MNRAS **416**, 832–856 (2011). 1105.3532.

623 76. Sault, R. J., Teuben, P. J. & Wright, M. C. H. A Retrospective View of MIRIAD. In Shaw,
624 R. A., Payne, H. E. & Hayes, J. J. E. (eds.) *Astronomical Data Analysis Software and Systems*
625 *IV*, vol. 77 of *Astronomical Society of the Pacific Conference Series*, 433 (1995). astro-ph/
626 0612759.

627 77. Swarup, G. *et al.* The Giant Metre-Wave Radio Telescope. *Current Science, Vol. 60,*
628 *NO.2/JAN25, P. 95, 1991* **60**, 95 (1991).

78. Cherukuri, S. V. *et al.* GRB 190114C: GMRT detection at 1.26GHz. *GRB Coordinates Network* **23762** (2019).

79. Tremou, L. *et al.* GRB 190114C: MeerKAT radio observation. *GRB Coordinates Network, Circular Service, No. 23760, #1 (2019)* **23760** (2019).

80. Camilo, F. *et al.* Revival of the Magnetar PSR J1622-4950: Observations with MeerKAT, Parkes, XMM-Newton, Swift, Chandra, and NuSTAR. ApJ **856**, 180 (2018). 1804.01933.

81. Jonas, J. & MeerKAT Team. The MeerKAT Radio Telescope. In *Proceedings of MeerKAT Science: On the Pathway to the SKA. 25-27 May*, 1 (2016).

82. Fender, R. *et al.* ThunderKAT: The MeerKAT Large Survey Project for Image-Plane Radio Transients. *arXiv e-prints* arXiv:1711.04132 (2017). 1711.04132.

83. Mohan, N. & Rafferty, D. PyBDSF: Python Blob Detection and Source Finder (2015). 1502.007.

84. Holland, W. S. *et al.* SCUBA-2: the 10 000 pixel bolometer camera on the James Clerk Maxwell Telescope. MNRAS **430**, 2513–2533 (2013). 1301.3650.

85. Bošnjak, Ž., Daigne, F. & Dubus, G. Prompt high-energy emission from gamma-ray bursts in the internal shock model. A&A **498**, 677–703 (2009). 0811.2956.

86. Panaitescu, A. & Kumar, P. Analytic Light Curves of Gamma-Ray Burst Afterglows: Homogeneous versus Wind External Media. ApJ **543**, 66–76 (2000). astro-ph/0003246.

647 87. Derishev, E. & Piran, T. The physical conditions of the afterglow implied by MAGIC's sub-
648 TeV observations of GRB 190114C. *arXiv e-prints* arXiv:1905.08285 (2019). 1905.08285.

649 88. Wang, X.-Y., Liu, R.-Y., Zhang, H.-M., Xi, S.-Q. & Zhang, B. Synchrotron self-Compton
650 emission from afterglow shocks as the origin of the sub-TeV emission in GRB 180720B and
651 GRB 190114C. *arXiv e-prints* arXiv:1905.11312 (2019). 1905.11312.

652 89. Mastichiadis, A. & Kirk, J. G. Self-consistent particle acceleration in active galactic nuclei.
653 A&A **295**, 613 (1995).

654 90. Vurm, I. & Poutanen, J. Time-Dependent Modeling of Radiative Processes in Hot Magnetized
655 Plasmas. ApJ **698**, 293–316 (2009). 0807.2540.

656 91. Petropoulou, M. & Mastichiadis, A. On the multiwavelength emission from gamma ray burst
657 afterglows. A&A **507**, 599–610 (2009). 0909.0208.

658 92. Pennanen, T., Vurm, I. & Poutanen, J. Simulations of gamma-ray burst afterglows with a
659 relativistic kinetic code. A&A **564**, A77 (2014). 1403.5506.

660 **Correspondence** Correspondence and requests for materials should be addressed to Razmik Mirzoyan
661 (email: razmik.mirzoyan@mpp.mpg.de) or MAGIC (email: magic@mpp.mpg.de).

662 **Author Contributions** The MAGIC telescope system was designed and constructed by the MAGIC Col-
663 laboration. Operation, data processing, calibration, Monte Carlo simulations of the detector, and of theo-
664 retical models, and data analyses were performed by the members of the MAGIC Collaboration, who also
665 discussed and approved the scientific results. L. Nava coordinated the gathering of the data, developed the

theoretical interpretation, and wrote the main section and the section on Afterglow Modeling. E. Moretti coordinated the analysis of the MAGIC data, wrote the relevant sections, and, together with F. Longo, coordinated the collaboration with the Fermi team. D. Miceli, Y. Suda and S. Fukami performed the analysis of the MAGIC data. S. Covino provided support with the analysis of the optical data and the writing of the corresponding sections. Z. Bosnjak performed calculations for the contribution from prompt emission to TeV radiation and wrote the corresponding section. S. Inoue, R. Mirzoyan, and A. Stamerra contributed in structuring and editing the paper. All MAGIC collaborators contributed to the editing and comments to the final version of the manuscript.

S. Campana and M. G. Bernardini extracted the spectra and performed the spectral analysis of *Swift*/BAT and *Swift*/XRT data. N. P. M. Kuin derived the photometry for the *Swift*/UVOT event mode data, and the uv grism exposure. M. H. Siegel derived the image mode Swift UVOT photometry. A. de Ugarte Postigo was principal investigator of ALMA program 2018.1A.00020.T, triggered these observations and performed photometry. S. Martin reduced the ALMA Band 6 data. C. C. Thöne, S. Schulze, D. A. Kann, and M. Michałowski participated in the ALMA DDT proposal preparation, observations, and scientific analysis of the data. D. A. Perley was principal investigator of ALMA program 2018.1.01410.T and triggered these observations, and was also principal investigator of the LT programme and the JCMT programme. A. M. Cockeram analyzed the ALMA Band 3 and LT data, and wrote the LT text. S. Schulze contributed to the development of the ALMA Band 3 observing programme. I. A. Smith triggered the JCMT programme, analyzed the data, and wrote the associated text. N. R. Tanvir contributed to the development of the JCMT programme. D. A. Kann and C. C. Thöne triggered and coordinated the X-shooter observations. D. A. Kann independently checked the optical light curve analysis.K. Misra was the principal investigator of the GMRT programme 35_018. S. V. Cherukuri and V. Jaiswal analyzed the data. L. Resmi contributed to the observation plan and data analysis. E.T., I.H. and R.D. have performed the MeerKAT data analysis. G. Anderson,

A. Moin, S. Schulze and E. Troja were principal investigator of ATCA program CX424. G. Anderson, M. Wieringa and J. Stevens carried out the observations. G. Anderson, G. Bernardi, S. Klose, M. Marongiu, A. Moin, R. Ricci and M. Wieringa analysed these data. M. Bell, J. Miller-Jones and L. Piro participated to the ATCA proposal preparation and scientific analysis of the data. The ePESSTO project was delivered by the following who have contributed to managing, executing, reducing, analysing ESO/NTT data and provided comments to the manuscript: J. P. Anderson, N. Castro Segura, P. D'Avanzo, M. Gromadzki, C. Inserra, E. Kankare, K. Maguire, M. Nicholl, F. Ragosta, S. J. Smartt. A. Melandri and A. Rossi reduced and analyzed REM data and provided comments to the manuscript. J. Bolmer was responsible for observing the GRB with GROND as well as for the data reduction and calibration. J. Bolmer and J. Greiner contributed to the analysis of the data and writing of the text. E. Troja triggered the *NuSTAR* TOO observations performed under DDT program, L. Piro requested the XMM-Newton data carried out under DDT program and carried out the scientific analysis of XMM-Newton and *NuSTAR*. S. Lotti analyzed the *NuSTAR* data and wrote the associated text. A. Tiengo and G. Novara analysed the XMM-Newton data and wrote the associated text. AJCT led the observing BOOTES and GTC programs. AC, CJPP, EFG, IMC, SBP and XYL analyzed the BOOTES data whereas AFV, MDCG, RSR, YDH and VVS analyzed the GTC data and interpreted them accordingly. N. Tanvir created the X-shooter and AlFOSC figures. J. Fynbo, J. Japelj performed the analysis of X-shooter and AlFOSC spectra. D. Xu, P. Jakobsson contributed to NOT programme and triggering. D. Malesani performed photometric analysis of NOT data.

Acknowledgements The MAGIC Collaboration would like to thank the Instituto de Astrofísica de Canarias for the excellent working conditions at the Observatorio del Roque de los Muchachos in La Palma. The financial support of the German BMBF and MPG, the Italian INFN and INAF, the Swiss National Fund SNF, the ERDF under the Spanish MINECO (FPA2017-87859-P, FPA2017-85668-P, FPA2017-82729-

711 C6-2-R, FPA2017-82729-C6-6-R, FPA2017-82729-C6-5-R, AYA2015-71042-P, AYA2016-76012-C3-1-P,
712 ESP2017-87055-C2-2-P, FPA201790566REDC), the Indian Department of Atomic Energy, the Japanese
713 JSPS and MEXT, the Bulgarian Ministry of Education and Science, National RI Roadmap Project DO1-
714 153/28.08.2018 and the Academy of Finland grant nr. 320045 is gratefully acknowledged. This work
715 was also supported by the Spanish Centro de Excelencia "Severo Ochoa" SEV-2016-0588 and SEV-2015-
716 0548, and Unidad de Excelencia "María de Maeztu" MDM-2014-0369, by the Croatian Science Foun-
717 dation (HrZZ) Project IP-2016-06-9782 and the University of Rijeka Project 13.12.1.3.02, by the DFG
718 Collaborative Research Centers SFB823/C4 and SFB876/C3, the Polish National Research Centre grant
719 UMO-2016/22/M/ST9/00382 and by the Brazilian MCTIC, CNPq and FAPERJ. L. Nava acknowledges
720 funding from the European Union's Horizon 2020 Research and Innovation programme under the Marie
721 Skłodowska-Curie grant agreement n. 664931. E. Moretti acknowledges funding from the European Union's
722 Horizon 2020 research and innovation programme under Marie Skłodowska-Curie grant agreement No
723 665919. This paper makes use of the following ALMA data:
724 ADS/JAO.ALMA#2018.A.00020.T, ADS/JAO.ALMA#2018.1.01410.T. ALMA is a partnership of ESO
725 (representing its member states), NSF (USA) and NINS (Japan), together with NRC (Canada), MOST and
726 ASIAA (Taiwan), and KASI (Republic of Korea), in cooperation with the Republic of Chile. The Joint
727 ALMA Observatory is operated by ESO, AUI/NRAO and NAOJ. CT, AdUP, and DAK acknowledge sup-
728 port from the Spanish research project AYA2017-89384-P. C. Thoene and A. de Ugarte Postigo acknowledge
729 support from funding associated to Ramón y Cajal fellowships (RyC-2012-09984 and RyC-2012-09975).
730 D. A. Kann acknowledges support from funding associated to Juan de la Cierva Incorporación fellowships
731 (IJCI-2015-26153). The James Clerk Maxwell Telescope is operated by the East Asian Observatory on
732 behalf of The National Astronomical Observatory of Japan; Academia Sinica Institute of Astronomy and
733 Astrophysics; the Korea Astronomy and Space Science Institute; Center for Astronomical Mega-Science (as

well as the National Key R&D Program of China with No. 2017YFA0402700). Additional funding support is provided by the Science and Technology Facilities Council of the United Kingdom and participating universities in the United Kingdom and Canada. The JCMT data reported here were obtained under project M18BP040 (P.I. D. Perley). We thank Mark Rawlings, Kevin Silva, Sheona Urquart, and the JCMT staff for the prompt support of these observations. The Liverpool Telescope, located on the island of La Palma in the Spanish Observatorio del Roque de los Muchachos of the Instituto de Astrofisica de Canarias, is operated by Liverpool John Moores University with financial support from the UK Science and Technology Facilities Council. The Australia Telescope Compact Array is part of the Australia Telescope National Facility which is funded by the Australian Government for operation as a National Facility managed by CSIRO. GEA is the recipient of an Australian Research Council Discovery Early Career Researcher Award (project number DE180100346) and JCAM-J is the recipient of Australian Research Council Future Fellowship (project number FT140101082) funded by the Australian Government. Support for the German contribution to GBM was provided by the Bundesministerium für Bildung und Forschung (BMBF) via the Deutsches Zentrum für Luft und Raumfahrt (DLR) under grant number 50 QV 0301. The UAH coauthors gratefully acknowledge NASA funding from cooperative agreement NNM11AA01A. C.A.W.H., and C.M.H. gratefully acknowledge NASA funding through the *Fermi*-GBM project.

The *Fermi* LAT Collaboration acknowledges generous ongoing support from a number of agencies and institutes that have supported both the development and the operation of the LAT as well as scientific data analysis. These include the National Aeronautics and Space Administration and the Department of Energy in the United States, the Commissariat à l'Energie Atomique and the Centre National de la Recherche Scientifique / Institut National de Physique Nucléaire et de Physique des Particules in France, the Agenzia Spaziale Italiana and the Istituto Nazionale di Fisica Nucleare in Italy, the Ministry of Education, Culture, Sports, Science and Technology (MEXT), High Energy Accelerator Research Organization (KEK) and

757 Japan Aerospace Exploration Agency (JAXA) in Japan, and the K. A. Wallenberg Foundation, the Swedish
758 Research Council and the Swedish National Space Board in Sweden.

759 Additional support for science analysis during the operations phase is gratefully acknowledged from the
760 Istituto Nazionale di Astrofisica in Italy and the Centre National d'Études Spatiales in France. This work
761 performed in part under DOE Contract DE-AC02-76SF00515.

762 Part of the funding for GROND (both hardware as well as personnel) was generously granted from the
763 Leibniz-Prize to Prof. G. Hasinger (DFG grant HA 1850/28-1). Swift data were retrieved from the Swift
764 archive at HEASARC/NASA-GSFC, and from the UK Swift Science Data Centre.

765 This work is based on observations obtained with XMM-Newton, an ESA science mission with instruments
766 and contributions directly funded by ESA Member States and NASA.

767 This work is partially based on observations collected at the European Organisation for Astronomical Re-
768 search in the Southern Hemisphere under ESO programme 199.D-0143. The work is partly based on ob-
769 servations made with the Gran Telescopio Canarias (GTC), installed in the Spanish Observatorio del Roque
770 de los Muchachos of the Instituto de Astrofísica de Canarias, in the island of La Palma. This work is par-
771 tially based on observations made with the Nordic Optical Telescope (programme 58-502), operated by the
772 Nordic Optical Telescope Scientific Association at the Observatorio del Roque de los Muchachos, La Palma,
773 Spain, of the Instituto de Astrofísica de Canarias. This work is partially based on observations collected at
774 the European Organisation for Astronomical Research in the Southern Hemisphere under ESO programme
775 102.D-0662. This work is partially based on observations collected through the ESO programme 199.D-
776 0143 ePESSTO. M. Gromadzki is supported by the Polish NCN MAESTRO grant 2014/14/A/ST9/00121.
777 M. Nicholl is supported by a Royal Astronomical Society Research Fellowship M. G. Bernardini, S. Cam-
778 pana, A. Melandri and P. D'Avanzo acknowledge ASI grant I/004/11/3. S. Campana thanks for support the

implementing agreement ASI-INAF n.2017-14-H.0. S. J. Smartt acknowledges funding from STFC Grant Ref: ST/P000312/1. NPMK acknowledges support by the UK Space Agency under grant ST/P002323/1 and the UK Science and Technology Facilities Council under grant ST/N00811/1. L. Piro, S. Lotti acknowledge partial support from the agreement ASI-INAF n.2017-14-H.0. VAF acknowledges RFBR 18-29-21030 for support. AJCT acknowledges support from the Junta de Andalucía (Project P07-TIC-03094) and support from the Spanish Ministry Projects AYA2012-39727-C03-01 and 2015-71718R. KM acknowledges the support from Department of Science and Technology (DST), Govt. of India and Indo-US Science and Technology Forum (IUSSTF) for the WISTEMM fellowship and Dept. of Physics, UC Davis where a part of this work was carried out. M.J.M. acknowledges the support of the National Science Centre, Poland through the grant 2018/30/E/ST9/00208. VJ and RL acknowledges support from the grant EMR/2016/007127 from Dept. of Science and Technology, India. K. Maguire acknowledges support from H2020 through an ERC Starting Grant (758638). L. Izzo would like to acknowledge Massimo Della Valle for invaluable support in the operation of the telescope.

Competing Interests The authors declare no competing interests.

Data Availability Statement Data are available from the corresponding authors upon request.

Code Availability Statement Proprietary data reconstruction codes were generated at the MAGIC telescopes large-scale facility. Information supporting the findings of this study are available from the corresponding authors upon request.

List of Figures